Optical Electrophysiology: Toward the Goal of Label-Free Voltage Imaging

Yuecheng Zhou, **Erica Liu**

Department of Chemistry, Stanford University, Stanford, California 94305, United States;

Holger Müller,

Department of Physics, University of California, Berkeley, California 94720, United States;
Molecular Biophysics and Integrated Bioimaging, Lawrence Berkeley National Laboratory,
Berkeley, California 94720, United States

Bianxiao Cui

Department of Chemistry, Stanford University, Stanford, California 94305, United States;

Abstract

Measuring and monitoring the electrical signals transmitted between neurons is key to understanding the communication between neurons that underlies human perception, information processing, and decision-making. While electrode-based electrophysiology has been the gold standard, optical electrophysiology has opened up a new area in the past decade. Voltage-dependent fluorescent reporters enable voltage imaging with high spatial resolution and flexibility to choose recording locations. However, they exhibit photobleaching as well as phototoxicity and may perturb the physiology of the cell. Label-free optical electrophysiology seeks to overcome these hurdles by detecting electrical activities optically, without the incorporation of exogenous fluorophores in cells. For example, electrochromic optical recording detects neuroelectrical signals via a voltage-dependent color change of extracellular materials, and interferometric optical recording monitors membrane deformations that accompany electrical activities. Label-free optical electrophysiology, however, is in an early stage, and often has limited sensitivity and temporal resolution. In this Perspective, we review the recent progress to overcome these hurdles. We hope this Perspective will inspire developments of label-free optical electrophysiology techniques with high recording sensitivity and temporal resolution in the near future.

1. INTRODUCTION

Modern electrophysiology has given us access to all levels of information from the *in vivo* cell activity in neural networks or cardiac muscles down to a single ion-channel in a cell membrane *in vitro*.[1] For example, neurons communicate with each other by encoding information in the form of action potentials.[2] Or, cardiac cells use action potentials to

regulate contraction and relaxation to form our beating heart.[3] This has led to numerous efforts dedicated to the development of electrophysiology with high fidelity and temporal resolution. Almost a century ago, Hodgkin and Huxley recorded the action potential inside the giant squid axon using a glass micropipet coupled with a silver wire.[2] Sakmann and Neher later developed the patch-clamp technique using a glass micropipet with a bath electrode, which has been the gold standard for measuring intracellular action potentials (Figure 1a).[4] A gigaohm seal is formed between the electrode and cell membrane, and intracellular action potentials can directly be recorded with a high signal-to-noise ratio (SNR) and high temporal resolution.[4] The recorded voltage waveforms and sub-threshold potentials often contain critical information about membrane ion-channels' activities, receptor–channel interactions, synaptic input, etc. However, the patch-clamp is invasive because it breaks the plasma membrane, which usually limits the recording to tens of minutes. In addition, the patch-clamp is laborious to apply and only records one or two cells simultaneously, despite recent efforts to increase the recording capacity through automated patch-clamping.[5–7] At the same time, extracellular recording methods using microelectrode arrays[8] (Figure 1b) are non-perturbative and allow parallel recording of multiple neurons in cultured neural networks and brain slices.[9,10] While extracellular recording methods are good at detecting action potential spikes, they do not report sub-threshold dynamics or allow precise manipulation of the cell such as current or voltage clamp. Recent advances in nanoelectrode arrays have further enabled intracellular recording by electroporation of the cell membrane through on-chip nanopillars.[11] However, prefabricated microelectrode arrays are still fixed in space and are inflexible to sense cells at user-selected spatial positions. To this end, sharp electrodes mounted on micromanipulators allow recording from targeted cells but suffer from low throughput like patch clamp.

By contrast, optical electrophysiology uses light as a sensor, which provides spatial flexibility in desired probing locations, avoids electrical wire connections with the specimen, allows imaging or multiplexed measurement, and affords a high spatial resolution.[1,12] A fluorescence indicator is usually required to optically detect neural activity.[13,14] The synthesis[15] and incorporation[16] of calcium indicators such as GCaMPs into cells have led to a burst in optical investigation of neural activity.[17–19] Calcium indicators are versatile and have good compatibility with fluorescence microscopy.[20,21] They can be engineered with tailored spectroscopic properties[22] and genetically encoded with fluorescent proteins to increase brightness and sensing accuracy.[23–25] Genetically encoded calcium indicators (GECIs) such as GCaMPs have been widely used for *in vivo* studies as they can be selectively expressed in a subset of neurons to dissect behavior-induced activities. Although modern calcium indicators can achieve ~25% fluorescence change ($\Delta F/F$) for a single action potential spike,[23] they rely on detecting the calcium ion concentration increase when voltage-gated calcium ion channels are activated by the action potential (Figure 1c). The temporal response of calcium indicators is on the order of hundreds of milliseconds and much slower than the action potential. The indirect measurement of the action potential through calcium peaks also makes it sometimes difficult to achieve a clear interpretation of the data.[13]

Voltage sensitive dye imaging captures action potential changes by inserting voltage sensitive dyes into the cell membrane[13,26,27] (Figure 1d). The transmembrane potential

change results in a spectral shift of the dye. In one class of dye, voltage-sensitivity arises via redistribution in chromophores or reorientation of dipole moment,[28] while another class exploits intrinsic electrochromic effects[29] or photoinduced electron transfer[30] for enhanced brightness and temporal resolution. Besides voltage-sensitive dyes, the rapid development of genetically encoded voltage indicators (GEVIs)[31–34] enables targeted expression of these probes in populations of neurons in cortical brain slices[35,36] or intact brains *in vivo*.[37] Similar to GECIs, GEVIs can be readily expressed in live animals and enable *in vivo* imaging of neuronal activities in a desired subset of neurons, which is a unique advantage of genetically encoded indicators and not shared by other approaches. One class of GEVI fuses a modified fluorescent protein into a transmembrane voltage-sensitive domain. The transmembrane voltage-sensitive domain inserts into the cell plasma membrane while the fluorescent protein remains outside[38] (Figure 1e). Over the years, this class of GEVIs has evolved to reach a maximum of 35% $\Delta F/F$ per 100 mV[39] with a response time of ~2 ms.[40] Another class of GEVIs uses the proton pump inside microbial rhodopsin, which changes fluorescence signals with membrane potential (Figure 1f).[41] This scaffold achieves ~90% $\Delta F/F$ per 100 mV with a response time of 0.05 ms.[42] Both GEVIs and voltage-sensitive dyes are able to record fast real-time intracellular action potential waveforms with high sensitivity as fluorescent reporters are directly inserted into the cell membrane. The performance of all GEVIs are reviewed comprehensively elsewhere.[43]

Despite these tremendous advantages, fluorescent voltage recording suffers from limited recording duration due to photobleaching.[44,45] Fluorescent imaging can generate phototoxic free radicals that may cause fast membrane depolarization.[46] The fluorescent reporters also need to be inserted into the cell plasma membrane,[13] which can potentially alter membrane electrical properties or even slow down the action potential conduction speed across the membrane.[47–49]

Label-free optical electrophysiology has caught the attention of researchers for decades. Ideally, label-free optical electrophysiology does not involve molecular probes and thus is non-perturbative and does not suffer from photobleaching or phototoxicity. Early efforts in label-free optical electrophysiology can be traced back to the 1940s when Hill and Keynes observed a decrease in light scattering signals for crab nerves stimulated in seawater.[50] Electrical activities of nerves or neurons were later confirmed to induce changes of intrinsic cell properties such as cell volume, light scattering intensity, or birefringence intensity, which were used to optically detect cell electrical activities in a label-free manner.[51,52] However, these changes are exceedingly small and thus hinder the detection accuracy and sensitivity of label-free optical electrophysiology despite more than 70 years of development.

The past decade has witnessed a rise in the development of label-free optical electrophysiology methods. In this Perspective, we review recent developments in label-free optical electrophysiology methods, focusing on three distinct approaches that convert electrical signals to optical readouts. The first approach is based on electrochromic or magnetochromic materials that convert electrical signals to color change of extracellular materials. The second approach is to optically detect miniscule membrane deformations that accompany cellular electric activities. The third approach is to detect changes in

light scattering, birefringence, and higher harmonic signals associated with cellular electric activities. We discuss the current state of the art and sensitivity limit in each approach, and close out the Perspective by providing outlooks toward new future directions in the field. We hope this Perspective will attract and knit together multidisciplinary interests from the field of chemistry, physics, and materials science to inspire continued development in this promising area of label-free optical electrophysiology.

2. LABEL-FREE OPTICAL ELECTROPHYSIOLOGY USING THIN FILMS OF ELECTROCHROMIC MATERIALS

The optical properties of electrochromic materials can be reversibly modulated by external voltages. Therefore, electrical signals from cells could locally change the optical properties of electrochromic materials if cells are within a close distance. Harnessing this unique electrochromic property is a new approach for optical detection of cell electrical signals. In this section, we discuss label-free optical electrophysiology techniques that achieve voltage imaging at the interface between the biological specimens and electrochromic thin films. These approaches are non-perturbative to the specimen and allow spatial flexibility in probing desired locations.

2.1. Monolayer Graphene for Optical Detection of Electric Fields.

Graphene is a promising candidate material for biosensing[53] and electrophysiology recording.[54] Being a single layer of carbon atoms in a 2D hexagonal lattice, graphene is mechanically stable, electrically conductive, and offers excellent biocompatibility.[55] Recent advances in understanding the optical properties of graphenes have further enabled graphene-based optoelectronic devices.[56] Graphene is an electrochromic material. The interband and optical transitions of graphenes were found to be tunable through electrical voltage gating such that the reflectance of the graphene can be modulated by electrical voltages.[56] Under this scheme, monolayer and bilayer graphene can reach a maximum of over 2% and 6% in light absorbance in the infrared (IR) region.[56] Horng et al. exploited this phenomenon to develop an electric field imaging platform based on critically coupled waveguide-amplified graphene.[57] On a prism-based total internal reflectance configuration, monolayer graphene grown through chemical vapor deposition is critically coupled with a planar waveguide composed of a layer of SiO_2 and a layer of Ta_2O_5 (Figure 2a). By applying the gate voltage through the gold electrode in contact with the graphene monolayer, the critical coupling condition[58] can be reached to drastically increase the detection sensitivity. When periodic square pulses with peak voltages of 500, 200, and 100 μV are applied to the graphene film, respective reflectivity changes of 0.58%, 0.23%, and 0.11% are recorded with bandwidth between 10 Hz and 10 kHz. For a 100 μV square wave, the SNR is ~6.5 (Figure 2b). The voltage imaging platform has an optical detection limit as small as ~15 μV, which should be sufficient to detect the extracellular action potential of neurons and cardiomyocytes.[59] However, graphene-based electrochromic detection requires ~0.6 V bias potential to enhance the sensitivity, which could be perturbative to cells. Detection of biological signals using graphene is yet to be demonstrated.

2.2. Thin Films of Electrochromic Polymers for Optical Detection of Action Potentials.

For most electrochromic materials, an externally applied voltage changes the optical properties through redox reactions where the reduced state and the oxidized state have different optical spectra. Metal oxides such as tungsten oxide or Prussian blue are the most widely used electrochromic materials, and they can be found in electrochromic smart windows, glass blinds, etc.[61] However, metal oxides have poor biocompatibility and stability in aqueous solutions under physiological conditions. On the other hand, conducting polymers containing π-conjugated motifs have gradually become a promising candidate material for next generation electrochromic sensors.[62] Conductive polymers can conjugate with biomolecules such as peptide residues for enhanced biocompatibility. Their mechanical properties could be tuned to match those of the biological tissues.[63,64] They can be easily processed into nanowires,[65] nanopillars,[66] or thin-film coating on microelectrodes for biological applications such as electrophysiology recording.[67]

Poly(3,4-ethylenedioxythiophene) (PEDOT) is a widely used conductive polymer. It is often mixed with polystyrenesulfonate (PSS) to form PEDOT:PSS. The mixture of the two conducting polyelectrolytes is water-soluble and easy for solution processing. PEDOT:PSS films possess high electrical conductivity of over 1000 s/cm^2 after treatment with chemicals such as ethylene glycol or dimethyl sulfoxide.[68] It is also biocompatible and chemically stable long-term under various biological buffer conditions. For example, electropolymerization of PEDOT:PSS around live neurons plated on a gold electrode was demonstrated feasible without significantly affecting cell viability.[69] Neural stem cells cultured on PEDOT:PSS film show elongated neurite growth when pulsed currents are applied to the film.[70] Human glioblastoma multiforme cell growth is facilitated on oxidized PEDOT:PSS film when a positive voltage is applied and primary human dermal fibroblasts prefer to grow on reduced PEDOT:PSS film when a negative voltage is applied.[71]

Nonetheless, conductive polymers are mostly used for their conductive properties and few works have focused on applications utilizing their electrochromic properties. Ranjbar et al. developed an immunosensor using electrodes coated with electrochromic polyaniline thin films. By applying a constant potential to the electrode, a baseline color change is induced in the polyaniline film when *E. coli* is captured by the thin film surface with antibodies.[72] Wu et al. also detected *S. aureus* in electrochromic π-conjugated copolymer solutions based on a similar concept.[73]

Recently, Alfonso and co-workers demonstrated a new approach named ElectroChromic Optical REcording (ECORE) to record cellular action potentials in a label-free manner by harnessing the electrochromic properties of PEDOT:PSS thin films.[60] In this approach, cells are cultured on electrodeposited PEDOT:PSS thin films. The s-polarized sample beam passes through the prism reaching the sample at 67° angle, 5° above the total internal reflectance angle. The reflected beam from the sample is then collected by a differential photodetector while the reference beam directly reaches the differential photodetector for laser noise reduction. When a cell fires an action potential, the electric signal locally modulates the optical absorption of the PEDOT:PSS film, which changes the film reflectance and is detected optically through a differential photodetector (Figure 2c). As shown in Figure 2d, when a 1 mV square wave is applied to the film in a cell-free

environment, ECORE detects a reflectance change of $\sim 3.0 \times 10^{-3}$ with a root-mean-square noise of less than 2.0×10^{-5}. ECORE has a voltage recording sensitivity of $\sim 6.7 \ \mu V$ with millisecond temporal resolution,[60] which is capable of recording individual action potentials of stem cell-derived cardiomyocytes (Figure 2e), rat hippocampal neurons (Figure 2f), and brain slices. An SNR as high as 41 was achieved for detecting single action potentials without any data averaging. ECORE offers the highest SNR among all optical electrophysiology methods and is already able to monitor neuronal activities in both cultured neurons and brain slices. As we discuss in later sections, other label-free methods often require averaging over hundreds of recording traces to improve SNR and are thus not suitable for detecting spontaneous electric activities from single neurons.

ECORE detects both the electrical signal and the mechanical signal as shown in the cardiomyocyte recording (Figure 2e). The electrical signal changes the color of the electrochromic thin film, while the mechanical signal changes the refractive index of the medium, both of which change the reflectance at the interface. The electric signal and the mechanical signal can be easily differentiated by their time scale, with electrical signals appearing as sharp spikes ~ 20 ms before the start of the mechanical contraction. With the capability of simultaneously detecting both electrical and mechanical signals,[74] ECORE could potentially enable new studies of excitation–contraction coupling in cardiomyocytes. So far, ECORE detects extracellular action potentials for a single cell. Further fast-scanning technology development is needed for ECORE to perform multi-site recording of many cells. More sensitive electrochromic materials can further be explored to enhance the recording sensitivity and temporal resolution of ECORE.[75]

2.3. Nitrogen-Vacancy Centers in Diamond Films for Sensing Action Potential-Induced Magnetic Fields.

Quantum diamond microscopy is a powerful tool for magnetic imaging of biological systems. Using atomic-scale quantum defects in diamond known as nitrogen-vacancy (NV) color centers,[76] quantum diamond microscopy senses and images magnetic fields through optically detected magnetic resonance (ODMR), which changes the fluorescence of the diamond containing NV color centers.[77–79] This technique enables imaging resolution of ~ 250 nm under ambient conditions and has recently been applied to image the magnetic field generated by magnetotactic bacteria[80] and tumor cells tagged with magnetic nanoparticles.[81]

The propagating action potential passing through the axon generates magnetic fields, which in theory can be detected by ODMR and used as a readout for label-free voltage imaging. However, the current associated with an action potential is extremely weak and the induced magnetic field is very small. Recently, Barry et al. was able to detect the extracellular action potential of invertebrate giant axons and intact live organism *Myxicola infundibulum* (worm) by sensing the accompanying magnetic field. The biological samples are placed directly on top of a 13-μm-thick single-crystal diamond chip doped with high density NV centers (Figure 2a).[82] When the magnetic fields generated by the specimen are close to a diamond surface containing NV centers, large Zeeman shifts of NV spin states are induced while the millisecond-scale NV electronic spin coherence time is still preserved. A wire

loop located above the diamond is used to apply microwave fields to manipulate the NV electronic spin coherence time. The NV spin states are then optically probed using a 532 nm green laser, and the laser-induced fluorescence in red is imaged onto a photodiode (Figure 3a inset). The magnetic field is detected using a continuous-wave electron spin resonance magnetometer[83] and the action potential is extracted from the time-dependent center spectrum shift of the ODMR signal.[82] The authors recorded the injection-triggered action potentials in worms and giant squid axons with a temporal resolution of ~32 μs. However, the measured SNR is approximately 1.2 for a single firing event of action potential. In order to improve the overall SNR, data averaging of 300–600 of triggered measurements on the same sample is needed (Figure 3b).[82] We note that this is an impressive achievement considering the miniscule magnetic field. Further technology developments are needed in order to detect individual action potentials.

3. LABEL-FREE OPTICAL ELECTROPHYSIOLOGY BY IMAGING MEMBRANE DEFORMATIONS INDUCED BY CELL ELECTRICAL ACTIVITIES

Neural electrical activity is a synergic process between all parts of the neurons including plasma membrane, ion channel proteins, axoplasm, etc. The generation of action potentials causes structural changes leading to fluctuations in cell membrane or volume.[51] Detecting these fluctuations has thus become the earliest and one of the widely explored approaches for label-free optical electrophysiology methods. In this section, we discuss recent efforts to image voltage through cell membrane deformations or volume changes.

3.1. Atomic Force Microscopy Shows Membrane Deformation Induced by Electrical Depolarization.

The phenomenological observation of action potential accompanied volume changes was first made in cuttlefish axons.[84] Since then, volume changes have been used as a probe to record neural action potentials. Using a mechanical bender with one end touching the nerves and the other end connected to a piezoelectric transducer, Tasaki and co-workers conducted a series of experiments and found the volume of non-myelinated nerve fibers expands a few nanometers laterally and shortens longitudinally during the firing of action potential in the 1980s.[85–88] Yao et al. confirmed this observation using an optical lever on stimulated lobster nerve bundles.[89] The authors found a rapid swelling of ~10 nm within 10 ms followed by a shrinking of ~100 nm in nerve bundle diameter by averaging over 100 traces.

Evolved from the mechanical bender and optical lever, atomic force microscopy (AFM) records cell membrane deformations with higher accuracy and sensitivity. For AFM, a tip is mounted underneath a cantilever and a laser beam is focused at the back of the cantilever. The reflected laser beam is collected by a photodetector to monitor the position of the cantilever in contact with the cell membrane.[90] AFM enables ultrasensitive detection of action potential induced membrane deformations with sub-nanometer resolution. Using AFM, Gonzalez-Perez et al. was able to detect action potentials of lobster giant axons (Figure 4a).[91] In a single recording trace, they were able to detect mechanical changes on the order of 0.2 to 1.2 nm. A higher SNR was further achieved after over 100 recording traces were averaged (Figure 4b).

Beyond invertebrate nerves and axons, Sachs and co-workers extended AFM-based detection of voltage-induced membrane deformations to mammalian cells using voltage-clamped HEK 293 cells transfected with *shaker* potassium ion channels (Figure 4c).[92,93] The cell membrane moves outward when depolarization potential is applied and inward when hyperpolarization potential is applied (Figure 4d).[92] The origin of voltage-induced membrane deformation is linked through the interaction between the interfacial tension and electrostatic potential. Changes in transmembrane potential cause local charge redistribution and lateral repulsion on the cell membrane. This leads to changes in local pressure and surface tension that result in membrane deformation (Figure 4c inset).[94] In another work,[95] Kim et al. recorded the nearly instantaneous mechanical spike that accompanies the action potential in intact mice neurohypophysis. The membrane swelling on the order of 5–10 nm was recorded using high bandwidth atomic force microscopy (HBAFM) with an SNR ~25 at 20 kHz sampling rate.[95] The swelling could again result from the voltage-induced membrane deformation, which is more significant in highly curved membranes such as nerve terminals.[92] On the other hand, the authors proposed another explanation that the pair of water molecules accompanying each sodium ion entering the neuron during the action potential caused the membrane to swell.

However, no direct experimental evidence has confirmed the physical origin of action potential induced membrane deformation and its underlying mechanism still remains elusive. Several computational studies have provided meaningful insights by establishing models that predict how action waves or pressure waves travel through the axonal membrane and axoplasmic fluid when neurons are excited.[96,97]

3.2. Imaging Voltage-Induced Membrane Deformations by Interferometric Microscopy.

Interferometric microscopy has gained its popularity in biological research for its high sensitivity and sub-nanometer resolution.[98,99] In interferometry, the illumination light is split into a signal beam that reaches the specimen and a reference beam that is reflected at a different surface. Nanometer-scale change in the optical path can be detected through phase changes when interferometric fringes are created by superimposing the signal beam with the reference beam. Two setup geometries are often adopted for interferometry. In a reflective geometry, both the signal beam and reference beam reach the specimen when the reflected light is collected. Since the beam double passes the specimen, larger measured phase changes are obtained with higher SNR, but the reflective process also reduces the light intensity reaching the detector leading to an increased phase noise.[100] Alternatively, transmission geometry allows spatial organization of optical signals from the entire specimen to be collected without relying on any hypothesized model to interpret the signal.[101]

Using interferometry, action potentials can be detected label-free through membrane shape fluctuations.[100–107] In 1977, Hill et al. detected a 1.8 nm change in crayfish giant axon diameter within 1 ms when an action potential passed along using a reflective geometry laser interferometer.[102] In 2004, Fang-Yen et al. measured the action potential-induced displacement of lobster walking leg nerves using a phase-referenced interferometer.[103] The optical signal indicates a peak swelling of ~5 nm for ~10 ms duration. In the same year,

Akkin et al. measured the leg nerve bundles of crayfish using low-coherence differential phase interferometer.[104] The authors reported less than 1 nm in the upward movement of the neural surface for 1 ms, matching the time scale for the arrival of action potential. LaPorta and Kleinfeld also reported an interferometric method by extracting phase changes from polarization signals rather than interferometric fringes to record the action potential in lobster walking leg nerves.[105] This method enables recording of membrane potential at a specific point on nerves but is limited to an optically thin specimen.

When nearly all interferometric recording of action potentials focus on invertebrate nerves and neurons, Oh et al. extended the study to mammalian cells in 2012.[101] The authors imaged the membrane potential of a single stimulated HEK 293 cell using a low-coherence diffraction phase microscope (LCDPM) which couples optical interferometry with microscopy. The transmission geometry and the common optical path design of LCDPM allows wide-field phase imaging of a single cell at 500 Hz (Figure 5a). At the same time, cell membrane deformations are imaged through the optical phase retardation of the light traversing a monolayer of cells (Figure 5b,c). The results indicate the optical signal of HEK 293 cells are from cell membrane deformations due to the direct coupling of membrane potential with membrane tension, which is in accordance with previous AFM studies.[92,93] Recently, Ling et al. also recorded the membrane potential of individual HEK 293 cells with improved temporal resolution through full-field interferometric imaging.[100]

Interferometry was further advanced to record the action potential from a single mammalian neuron, which requires even higher optical path length sensitivity and temporal resolution.[106] In 2020, Ling et al. performed full-field interferometric voltage imaging on mouse cortical neurons plated on a transparent MEA substrate (Figure 5d).[107] Using this method, information regarding action potential induced cell deformation of the entire cell and the corresponding neural network could be retrieved. The authors achieved 0.1 ms temporal resolution and axial path length sensitivity of 4 pm/pixel. In a representative experiment, mouse cortical neuron somas showed deformation between 1.8 nm shrinkage to 1.3 nm swelling and mouse cortical neuron neurites showed 0.7 nm shrinkage to 0.9 nm swelling when the action potential propagated through (Figure 5e).[107] The authors also reduced the recording noise level and achieved an SNR of 21.5 by averaging over 7500 neuron spikes using a data analysis method termed spike-triggered averaging (STA). This method synchronizes thousands of recorded phase movies on the same population of neurons based on the beginning neuron spiking time obtained from MEA recording as the recording noise level scales with $1/\sqrt{N}$, where N is the number of neuronal spikes from recorded phase movies (Figure 5f).

3.3. Imaging Voltage-Induced Membrane Deformations by Surface Plasmon Resonance Microscopy.

Surface plasmon resonance (SPR) is the collective oscillation of conducting electrons at the interface of metals (negative real part permittivity) and dielectric materials (positive real part permittivity) when optically stimulated using visible or near-infrared light. The most widely used optical configuration to excite surface plasmons is the Kretschmann configuration.[108] Incident light that passes through a prism coupler[108] or a high numerical

aperture objective[109] at the total internal reflectance (TIR) angle generates an evanescent wave penetrating the metal film (gold or silver) in contact. The evanescent field of surface plasmons probes the surface of the metal film such that any changes on the surface alter the propagation constant of the surface plasmons. Changes in propagation constant then result in changes in reflective angle, intensity or phase of the coupled light wave.[110] SPR is the most sensitive to activity at the vicinity of the metal surface because the plasmon evanescent wave decays exponentially perpendicular to the surface.

SPR has widely been used in chemical and biosensing because of its high detection sensitivity near the metal surface.[110] In 2008, Kim et al. made a label-free imaging of the electrical activity of mouse sciatic nerves in contact with a gold substrate through nerve membrane fluctuations using prism-based SPR (Figure 6a).[111] The SPR signal from the propagating action potential along the nerve was measured through the intensity change of the outcoming beam using a photodetector. The authors were able to record the action potential with an SNR ~4 before signal averaging (Figure 6b).

SPR can further be exploited for imaging. Modern objective-based TIR microscopy renders surface plasmon resonance suitable for imaging. It has been used to investigate cellular processes[112,113] and track nano- to micrometer sized biological particles.[114,115] The Nongjian Tao group developed the plasmon-based electrochemical impedance microscopy that enables wide-field imaging of electrochemical impedance distribution at the interface between gold films and biological specimens.[116] When a potential modulation is applied to the SPR interface, a change in surface charge density leads to a change in the dielectric constant of the metal layer. Then the impedance image containing both the amplitude and phase information on the sample under different potential modulation frequencies are recorded through a camera synchronized with the potential and current modulation, and analyzed using a Fourier transform algorithm.[117] Using this method, an impedance measurement could be achieved with sub-millisecond temporal resolution and sub-micrometer spatial resolution.[116–118]

Using plasmon-based electrochemical impedance microscopy, Liu et al. performed high-resolution label-free imaging and recording of the propagating action potential in a mouse hippocampal neuron cultured on ~50 nm gold film at 10 kHz frame rate (Figure 6c).[120] The authors initially attributed the measured signal to the charge density variation on the gold film induced by the transient local field potential,[120] but later clarified the signal to originate from the action potential-induced membrane fluctuation.[119] By tracking the cell membrane movement, Yang et al. observed sub-nanometer membrane movement associated with the action potential ranging from 0.2 to 0.4 nm (Figure 6d). The SNR of the measured transient membrane displacement is approximately 7 and its time-dependent profile matches well with the simultaneous recorded action potential using patch clamp.[119] In a subsequent work, the authors investigated the cytoplasm and cytoskeleton mechanical properties of HEK 293T cells under membrane electromechanical deformation. They have found that local variations in membrane deformation is closely related to cell–substrate interactions.[121] We direct the readers to a review elsewhere for more applications of SPR and plasmon-based electrochemical impedance microscopy other than label-free optical electrophysiology.[122]

4. LABEL-FREE OPTICAL ELECTROPHYSIOLOGY BY DETECTING CELL INTRINSIC OPTICAL SIGNALS

The structural deformation, volume change, and membrane fluctuation in nerves and neurons also lead to changes in cell intrinsic optical signals such as light scattering intensity, birefringence intensity, etc. In this section, we review label-free optical electrophysiology methods relying on detecting these signal changes and are non-contact to the specimen.

4.1. Microscopy Detecting Light Scattering Changes.

In 1949, Hill and Keynes first found that the white-light scattering intensity changes for crab limb nerves after trains of external stimuli were applied.[50] In the 1970s, Cohen and colleagues later confirmed this in studies with different types of non-myelinated nerves and giant axons of invertebrates.[51,123–126] In their studies, light scattering change was found to depend on the charge passing through the nerve or giant axon.[125,126] Almost 20 years later in 1991, the propagation of a transmembrane potential along the axon of *cultured* neurons of *Aplysia californica* were recorded using dark-field microscopy.[127] The authors achieved an SNR of 5–10 without data averaging. The induced scattering changes were attributed to the alignment of membrane dipoles along the direction of the transmembrane electrical field. The neuron scattering change was also found to depend linearly on the transmembrane potential rather than the current, in contrast to the finding by Cohen et al.[125,126]

Optical coherence tomography (OCT) and optical coherence microscopy (OCM) allow detection of scattered light from biological specimens.[128–131] In 2009, Boppart and colleagues imaged the electrical activities of *A. californica* neurons using spectral domain (SD) OCT/OCM.[132] In SD-OCT/OCM, a broadband laser reflected from the sample arm is combined with the light from the reference arm to create an interference pattern and spectrally resolved through a spectrometer (Figure 7a). A depth-dependent light scattering profile (wavelength domain) is obtained from the interference pattern (spatial frequency domain) through inverse Fourier transformation.[132] The authors used OCT to detect the scattering change from multiple neurons situated in *A. californica* abdominal ganglion at different depths, and OCM to detect the backscattered light from a single cultured bag cell neuron with higher spatial resolution. From the OCM image, the authors observed an increase in scattering intensity for a single neuron when an electrical stimulus is applied, which correlated well with the transmembrane potential changes (Figure 7b).[132]

Electrical activities of mammalian cells were also imaged through light scattering. Using bright-field microscopy coupled with a multi-element photodiode array, Salzberg et al. recorded the intrinsic scattering changes in the terminals of stimulated mouse neurohypophysis in order to shed light on neuro-secretory behaviors.[134] In addition to the arrival of the electrical impulse, a large component of the optical change was found to correspond to an early event of neuropeptide release. Using dark-field microscopy, light scattering signals were also recorded in stimulated mouse coronal neocortical brain slices.[135] Recently, Habib et al. developed an electroplasmonic nanoantenna array by selectively polymerizing electrochromic polymers on top of the gold nanoelectrodes patterned on a indium tin oxide (ITO) substrate.[133] Dark-field microscopy was again applied to image

the electrical activity of cardiomyocyte networks cultured on a nanoantenna array. Low intensity white light (11 mW/mm^2) passing through the dark field condenser reaches the nanoantenna array and the transmitted far-field scattering signal collected by an objective was detected using a spectrometer (Figure 7c). Enhanced interactions between light and each electroplasmonic nanoantenna are exploited to achieve fast electro-optic sensing. Under 1 V and 200 Hz external voltage modulation in a cell free system, the light scattering signal changes with a high signal-to-noise ratio and a switching time of 191 μs (Figure 7d).

4.2.   Microscopy Detecting Birefringence Changes.

Birefringence is closely related to the structural order of the material. It originates from the difference in refractive indices of a material in directions perpendicular and parallel to the direction of the light pass through. Birefringence has become an important measure of the optical property for biological tissues consisting of various structural components that are highly anisotropic.

The birefringence or the optical retardation (product of birefringence and sample thickness) was first reported to change in crab nerves and giant squid axons when electrical impulses passed through.[123,136] The action potential in the lobster walking leg nerve was later recorded in real-time by illuminating the sample nerves using polarized incident light. The transmitted light passing through a linear polarizer orthogonal to the incident light polarizer was then detected. In this way, the cross-polarized signal was maximized and nerve birefringence change was used to record the action potential.[137–139] Compared to light scattering signals, birefringence signals exclude the non-specific scattering in tissues that could cause noise or artifacts.[140] Hence, monitoring changes in birefringence could potentially be a "cleaner" method to optically record action potentials in a label-free manner. However, birefringence imaging has yet to be applied to record electrical activities of mammalian cells.

4.3.   Higher Harmonic Generation Microscopy.

Since the beginning of this century, higher harmonic generation (HHG) microscopy has started to gain popularity in biological research.[141] Compared to single-photon fluorescence microscopy, HHG microscopy allows deeper penetration into the tissue with axial sectioning capabilities by relying on nonlinear optical signals, which are less susceptible to noise from optical interference, especially in deep tissue. Ideally, HHG microscopy, including second-order harmonic generation (SHG) microscopy and third-order harmonic generation (THG) microscopy, leaves no excessive heat to the specimen because the energy carried away by the outgoing photon equals the total energy of the ingoing photons.[141] This mechanism allows low photo-damage to the biological specimen without depositing any extra energy.

SHG involves a multi-photon process where two input photons are converted into one excited photon at twice the initial frequency after interacting with the specimen. The SHG signal can only be generated in noncentrosymmetric medium. It is coupled to the surface-induced nonlinear polarization. The power $P^{\mathrm{NL}}(2\omega)$ of the second harmonic depends on the square of the input light intensity such that $P^{\mathrm{NL}}(2\omega) \sim \chi^{(2)} E(\omega)_1 E(\omega)_2$, where $\chi^{(2)}$ is the second-order surface susceptibility to the applied laser-induced electrical field $E(\omega)$.

Similarly, THG involves a multi-photon process and the THG signal intensity depends on the cubic of the input light intensity such that $P^{NL}(3\omega) \sim \chi^{(3)}E(\omega)_1E(\omega)_2E(\omega)_3$, where $\chi^{(3)}$ is the third-order surface susceptibility. Thus, HHG becomes a promising method for label-free imaging of biological specimens that contain noncentrosymmetric matters[142] or have a high third-order surface susceptibility.[143] Chen et al. conducted long-term observation of the development of zebrafish embryonic nervous systems combining SHG and THG.[142] Witte et al. enhanced the THG signal through partial phase matching by tuning the THG excitation laser focal volume in order to explore the geometry and lipid content in mouse cortex brain slices.[144]

However, special consideration is needed for label-free voltage-imaging using HHG. When interfacial chemical or electrostatic interactions take place for dipolar molecules, their distribution becomes noncentrosymmetric and generates SHG signals. Since water is the most abundant dipolar molecule at the aqueous interface and its orientation distribution can be altered by interfacial electrostatic interactions, it is an ideal probe molecule.[145] Using high-throughput SHG microscopy, Roke and colleagues imaged the transmembrane potential of liposomes[146] and free-standing bilipid membranes[147] in aqueous solutions under various ionic strengths and external electrical fields. The SHG signals arose from the hydrating water molecules at lipid bilayer surfaces when the water molecules were reoriented by the charge-dipole interactions between water dipoles and charged lipid head groups.[147] Since cell plasma membrane is also a lipid bilayer, the authors further imaged mouse cortical neuron membrane potentials using water as the probe molecule and achieved an SNR of 4 with an acquisition time of 100 ms (Figure 8a).[148] After increasing the extracellular potassium ions concentration, the SHG signal of potassium induced membrane voltage change was recorded for three cell bodies. Spatial heterogeneities during the depolarization step were also observed (Figure 8b). Specifically, membrane potentials are more positive in the somas than neurites and vice versa during the recovery step. The spatially averaged SHG signal and the calculated corresponding membrane voltage is shown in Figure 8c. Both traces decrease during the depolarization step followed by an increase at the recovery step.[148] SHG microscopy is able to provide real-time transmembrane potential mapping, but limited by the temporal resolution on the order of 100 ms. Thus, the detection of action potentials by SHG is yet to be achieved.

4.4. Stimulated Raman Scattering Microscopy.

Raman spectroscopy measures molecular spectra to fingerprint different chemical species. In Raman spectroscopy, the sample is excited using visible light and different vibrational modes of the molecule are extracted from the scattered light detected.[149] Raman scattering has weak scattering signals and a small scattering cross-section. A high power excitation light source is often needed and the imaging speed is also limited for detection of fast live cell dynamics.[150] Stimulated Raman scattering (SRS) microscopy offers nearly identical spectral profiles to spontaneous Raman spectroscopy, but offers orders of magnitude stronger signals linearly related to molecular concentration. It is also free of nonresonant background, making it a powerful tool for quantitative chemical imaging and bioimaging in a label-free manner.[151,152]

Using SRS microscopy, Liu et al. measured the vibrational spectrum of the ghost erythrocyte membrane as a function of applied potential.[154] The normalized SRS signal at ~2930 cm^{-1} (with respect to the intensity band at ~2850 cm^{-1}) increases by ~2.6 times when membrane potential changes from −10 to +10 mV. This signal primarily originated from the −CH$_3$ groups in membrane proteins.[154] Lee and Zhang et al. further applied SRS microscopy to image the action potential of mouse cortical neurons label-free (Figure 9a) with an SNR ~ 3.6 without data averaging (Figure 9b) through the intensity change of Raman shift at ~2930 cm^{-1} (Figure 9c).[153] The authors proposed that the change in SRS signal intensity is related to sodium ion activity during the depolarization step since the change in spectrum intensity was significantly reduced when tetrodotoxin (TTX) was used to block the sodium ion channels (Figure 9d). SRS microscopy can further be optimized by enhancing the line scanning and data acquisition speed to achieve millisecond temporal resolution for label-free optical electrophysiology. We refer the readers to a review elsewhere for more details.[155]

5. SUMMARY AND OUTLOOK

Label-free optical electrophysiology is an emerging field full of possibilities. Cell electrical signals can be imaged at the interface between biological specimens and electrochromic thin films. Quantum diamond microscopy images the magnetic field accompanied by the action potential through the fluorescence change of diamond films containing NV color centers, albeit requiring data averaging. ElectroChromic Optical Recording (ECORE) detects neuroelectrical signals with a high SNR without data averaging via monitoring the voltage-dependent color change of extracellular electrochromic polymers. Moreover, cell electrical activities can also induce membrane deformations and intrinsic optical signal changes, which can be utilized as probes for label-free voltage imaging. Major recent advances in label-free optical electrophysiology relying on different sensing mechanisms are summarized in Table 1.

Nevertheless, further developments for label-free optical electrophysiology are still needed with regards to the SNR, spatial-temporal resolution, and measurement throughput. Most current label-free voltage imaging techniques, except for ECORE and interferometric imaging, still require data averaging for detecting mammalian neurons. It is therefore desirable to improve the SNR in order to detect single action potentials with high fidelity. For ECORE, it is of significant interest to extend the voltage imaging throughput from one cell to multi-site recording of a population of cells by scanning the probing beam. In this way, the collective electrical activities of cells within a large region of interest can be investigated. For high-harmonic and Raman scattering microscopies, in addition to the need for improving SNR, a millisecond detection temporal sensitivity is yet to be achieved. For dark field microscopy with nanoantenna, the signal-to-noise ratio could be improved with more studies of the underlying mechanisms. These improvements in label-free optical electrophysiology can be achieved through further developments in optical detection methods and advances in new electrochromic materials. Furthermore, those label-free optical electrophysiology techniques with different advantages could potentially be combined in order to achieve the best voltage imaging performance.

So far, label-free optical electrophysiology methods have yet to be applied for *in vivo* voltage imaging in the brain.[156] This remains challenging because the brain tissue acts as a large scattering medium and the weak cell intrinsic signals are often buried in the background noise. Nonlinear multiphoton imaging modalities such as SHG or THG, which are able to image deep into the tissue,[144,157] could potentially be used to overcome this hurdle. However, their temporal resolution needs to be enhanced in order to record a single action potential.[158] Voltage imaging using long wavelength illumination in the IR region can also be an option to record electrical signals millimeter deep into the brain.[159] Another promising tool for future label-free voltage imaging *in vivo* is ECORE. Its optical components can potentially be miniaturized and coupled with fiber micro-endoscopy for *in vivo* voltage recording.[160,161] Label-free optical electrophysiology could be integrated with optogenetics[162] to control and image neuronal activities in a circuit.[163] Since no fluorescent reporters are required for label-free optical recording, more intricate stimulation or inhibition schemes on neurons can be applied without worrying about possible optical crosstalk between the signal readout channel and the manipulating channel.

ACKNOWLEDGMENTS

REFERENCES

(1). Scanziani M; Häusser M Electrophysiology in the Age of Light. Nature 2009, 461 (7266), 930–939. [PubMed: 19829373]

(2). Hodgkin AL; Huxley AF Action Potentials Recorded from Inside a Nerve Fibre. Nature 1939, 144, 710–711.

(3). Peng S; Lacerda AE; Kirsch GE; Brown AM; Bruening-Wright A The Action Potential and Comparative Pharmacology of Stem Cell-Derived Human Cardiomyocytes. J. Pharmacol. Toxicol. Methods 2010, 61, 277–286. [PubMed: 20153443]

(4). Sakmann B; Neher E Patch Clamp Techniques for Studying Ionic Channels in Excitable Membranes. Annu. Rev. Physiol 1984, 46, 455–472. [PubMed: 6143532]

(5). Sakmann B; Neher E Geometric Parameters of Pipettes and Membrane Patches. Single-Channel Recording 1995, 637–650.

(6). Kitamura K; Judkewitz B; Kano M; Denk W; Häusser M Targeted Patch-Clamp Recordings and Single-Cell Electroporation of Unlabeled Neurons in Vivo. Nat. Methods 2008, 5, 61–67. [PubMed: 18157136]

(7). Kodandaramaiah SB; Franzesi GT; Chow BY; Boyden ES; Forest CR Automated Whole-Cell Patch-Clamp Electrophysiology of Neurons in Vivo. Nat. Methods 2012, 9, 585–587. [PubMed: 22561988]

(8). Pine J Recording Action Potentials from Cultured Neurons with Extracellular Microcircuit Electrodes. J. Neurosci. Methods 1980, 2, 19–31. [PubMed: 7329089]

(9). Jones IL; Livi P; Lewandowska MK; Fiscella M; Roscic B; Hierlemann A The Potential of Microelectrode Arrays and Microelectronics for Biomedical Research and Diagnostics. Anal. Bioanal. Chem 2011, 399, 2313–2329. [PubMed: 20676620]

(10). Spira ME; Hai A Multi-Electrode Array Technologies for Neuroscience and Cardiology. Nat. Nanotechnol 2013, 8, 83–94. [PubMed: 23380931]

(11). Xie C; Lin Z; Hanson L; Cui Y; Cui B Intracellular Recording of Action Potentials by Nanopillar Electroporation. Nat. Nanotechnol 2012, 7, 185–190. [PubMed: 22327876]

(12). Wilt BA; Burns LD; Ho ETW; Ghosh KK; Mukamel EA; Schnitzer MJ Advances in Light Microscopy for Neuroscience. Annu. Rev. Neurosci 2009, 32, 435–506. [PubMed: 19555292]

(13). Peterka DS; Takahashi H; Yuste R Imaging Voltage in Neurons. Neuron 2011, 69 (1), 9–21. [PubMed: 21220095]

(14). Emiliani V; Cohen AE; Deisseroth K; Häusser M All-Optical Interrogation of Neural Circuits. J. Neurosci 2015, 35 (41), 13917–13926. [PubMed: 26468193]

(15). Tsien RY New Calcium Indicators and Buffers with High Selectivity against Magnesium and Protons: Design, Synthesis, and Properties of Prototype Structures. Biochemistry 1980, 19, 2396–2404. [PubMed: 6770893]

(16). Tsien RY A Non-Disruptive Technique for Loading Calcium Buffers and Indicators into Cells. Nature 1981, 290, 527–528. [PubMed: 7219539]

(17). Salzberg BM; Obaid AL; Senseman DM; Gainer H Optical Recording of Action Potentials from Vertebrate Nerve Terminals Using Potentiometric Probes Provides Evidence for Sodium and Calcium Components. Nature 1983, 306, 36–40. [PubMed: 6633657]

(18). Salzberg BM; Obaid AL; Gainer H Optical Studies of Excitation and Secretion in Vertebrate Nerve Terminals. Topics in the Neurosciences 1986, 1, 259–259.

(19). Yuste R; Denk W Dendritic Spines as Basic Functional Units of Neuronal Integration. Nature 1995, 375, 682–684. [PubMed: 7791901]

(20). Stosiek C; Garaschuk O; Holthoff K; Konnerth A In Vivo Two-Photon Calcium Imaging of Neuronal Networks. Proc. Natl. Acad. Sci. U. S. A 2003, 100, 7319–7324. [PubMed: 12777621]

(21). Göbel W; Helmchen F In Vivo Calcium Imaging of Neural Network Function. Physiology 2007, 22, 358–365. [PubMed: 18073408]

(22). Grynkiewicz G; Poenie M; Tsien RY A New Generation of Ca2+ Indicators with Greatly Improved Fluorescence Properties. J. Biol. Chem 1985, 260 (6), 3440–3450. [PubMed: 3838314]

(23). Chen T-W; Wardill TJ; Sun Y; Pulver SR; Renninger SL; Baohan A; Schreiter ER; Kerr RA; Orger MB; Jayaraman V; Looger LL; Svoboda K; Kim DS Ultrasensitive Fluorescent Proteins for Imaging Neuronal Activity. Nature 2013, 499, 295–300. [PubMed: 23868258]

(24). Miyawaki A; Llopis J; Heim R; McCaffery JM; Adams JA; Ikura M; Tsien RY Fluorescent Indicators for Ca2 Based on Green Fluorescent Proteins and Calmodulin. Nature 1997, 388, 882–887. [PubMed: 9278050]

(25). Thestrup T; Litzlbauer J; Bartholomäus I; Mues M; Russo L; Dana H; Kovalchuk Y; Liang Y; Kalamakis G; Laukat Y; Becker S; Witte G; Geiger A; Allen T; Rome LC; Chen T-W; Kim DS; Garaschuk O; Griesinger C; Griesbeck O Optimized Ratiometric Calcium Sensors for Functional in Vivo Imaging of Neurons and T Lymphocytes. Nat. Methods 2014, 11, 175–182. [PubMed: 24390440]

(26). Tsytsarev V; Liao L-D; Kong KV; Liu Y-H; Erzurumlu RS; Olivo M; Thakor NV Recent Progress in Voltage-Sensitive Dye Imaging for Neuroscience. J. Nanosci. Nanotechnol 2014, 14 (7), 4733–4744. [PubMed: 24757943]

(27). Kulkarni RU; Miller EW Voltage Imaging: Pitfalls and Potential. Biochemistry 2017, 56, 5171–5177. [PubMed: 28745864]

(28). Ehrenberg B; Montana V; Wei MD; Wuskell JP; Loew LM Membrane Potential Can Be Determined in Individual Cells from the Nernstian Distribution of Cationic Dyes. Biophys. J 1988, 53, 785–794. [PubMed: 3390520]

(29). Fluhler E; Burnham VG; Loew LM Spectra, Membrane Binding, and Potentiometric Responses of New Charge Shift Probes. Biochemistry 1985, 24 (21), 5749–5755. [PubMed: 4084490]

(30). Huang Y-L; Walker AS; Miller EW A Photostable Silicon Rhodamine Platform for Optical Voltage Sensing. J. Am. Chem. Soc 2015, 137 (33), 10767–10776. [PubMed: 26237573]

(31). Knöpfel T Genetically Encoded Optical Indicators for the Analysis of Neuronal Circuits. Nat. Rev. Neurosci 2012, 13 (10), 687–700. [PubMed: 22931891]

(32). St-Pierre F; Chavarha M; Lin MZ Designs and Sensing Mechanisms of Genetically Encoded Fluorescent Voltage Indicators. Curr. Opin. Chem. Biol 2015, 27, 31–38. [PubMed: 26079047]

(33). Lin MZ; Schnitzer MJ Genetically Encoded Indicators of Neuronal Activity. Nat. Neurosci 2016, 19 (9), 1142–1153. [PubMed: 27571193]

(34). Xu Y; Zou P; Cohen AE Voltage Imaging with Genetically Encoded Indicators. Curr. Opin. Chem. Biol 2017, 39, 1–10. [PubMed: 28460291]

(35). Akemann W; Mutoh H; Perron A; Park YK; Iwamoto Y; Knöpfel T Imaging Neural Circuit Dynamics with a Voltage-Sensitive Fluorescent Protein. J. Neurophysiol 2012, 108, 2323–2337. [PubMed: 22815406]

(36). Fan LZ; Nehme R; Adam Y; Jung ES; Wu H; Eggan K; Arnold DB; Cohen AE All-Optical Synaptic Electrophysiology Probes Mechanism of Ketamine-Induced Disinhibition. Nat. Methods 2018, 15 (10), 823–831. [PubMed: 30275587]

(37). Akemann W; Mutoh H; Perron A; Rossier J; Knöpfel T Imaging Brain Electric Signals with Genetically Targeted Voltage-Sensitive Fluorescent Proteins. Nat. Methods 2010, 7 (8), 643–649. [PubMed: 20622860]

(38). Siegel MS; Isacoff EY A Genetically Encoded Optical Probe of Membrane Voltage. Neuron 1997, 19, 735–741. [PubMed: 9354320]

(39). Jin L; Han Z; Platisa J; Wooltorton JRA; Cohen LB; Pieribone VA Single Action Potentials and Subthreshold Electrical Events Imaged in Neurons with a Fluorescent Protein Voltage Probe. Neuron 2012, 75 (5), 779–785. [PubMed: 22958819]

(40). St-Pierre F; Marshall JD; Yang Y; Gong Y; Schnitzer MJ; Lin MZ High-Fidelity Optical Reporting of Neuronal Electrical Activity with an Ultrafast Fluorescent Voltage Sensor. Nat. Neurosci 2014, 17 (6), 884–889. [PubMed: 24755780]

(41). Kralj JM; Hochbaum DR; Douglass AD; Cohen AE Electrical Spiking in Escherichia Coli Probed with a Fluorescent Voltage-Indicating. Science 2011, 333 (6040), 345–348. [PubMed: 21764748]

(42). Hochbaum DR; Zhao Y; Farhi SL; Klapoetke N; Werley CA; Kapoor V; Zou P; Kralj JM; Maclaurin D; Smedemark-Margulies N; Saulnier JL; Boulting GL; Straub C; Cho YK; Melkonian M; Wong GK-S; Harrison DJ; Murthy VN; Sabatini BL; Boyden ES; Campbell RE; Cohen AE All-Optical Electrophysiology in Mammalian Neurons Using Engineered Microbial Rhodopsins. Nat. Methods 2014, 11, 825–833. [PubMed: 24952910]

(43). Bando Y; Sakamoto M; Kim S; Ayzenshtat I; Yuste R Comparative Evaluation of Genetically Encoded Voltage Indicators. Cell Rep. 2019, 26 (3), 802–813. [PubMed: 30650368]

(44). Grandy TH; Greenfield SA; Devonshire IM An Evaluation of in Vivo Voltage-Sensitive Dyes: Pharmacological Side Effects and Signal-to-Noise Ratios after Effective Removal of Brain-Pulsation Artifacts. J. Neurophysiol 2012, 108 (11), 2931–2945. [PubMed: 22972958]

(45). Mennerick S; Chisari M; Shu H-J; Taylor A; Vasek M; Eisenman LN; Zorumski CF Diverse Voltage-Sensitive Dyes Modulate GABAA Receptor Function. J. Neurosci 2010, 30 (8), 2871–2879. [PubMed: 20181584]

(46). Hirase H; Nikolenko V; Goldberg JH; Yuste R Multiphoton Stimulation of Neurons. J. Neurobiol 2002, 51, 237–247. [PubMed: 11984845]

(47). Blunck R; Chanda B; Bezanilla F Nano to Micro — Fluorescence Measurements of Electric Fields in Molecules and Genetically Specified Neurons. J. Membr. Biol 2005, 208, 91–102. [PubMed: 16645739]

(48). Baker BJ; Mutoh H; Dimitrov D; Akemann W; Perron A; Iwamoto Y; Jin L; Cohen LB; Isacoff EY; Pieribone VA; Hughes T; Knöpfel T Genetically Encoded Fluorescent Sensors of Membrane Potential. Brain Cell Biol. 2008, 36, 53–67. [PubMed: 18679801]

(49). Maclaurin D; Venkatachalam V; Lee H; Cohen AE Mechanism of Voltage-Sensitive Fluorescence in a Microbial Rhodopsin. Proc. Natl. Acad. Sci. U. S. A 2013, 110, 5939–5944. [PubMed: 23530193]

(50). Hill DK; Keynes RD Opacity Changes in Stimulated Nerve. J. Physiol 1949, 108, 278–281.

(51). Cohen LB Changes in Neuron Structure during Action Potential Propagation and Synaptic Transmission. Physiol. Rev 1973, 53 (2), 373–418. [PubMed: 4349816]

(52). Cohen L Special Topic: Optical Approaches to Neuron Function. Annu. Rev. Physiol 1989, 51, 487–490. [PubMed: 2712540]

(53). Wu L; Chu HS; Koh WS; Li EP Highly Sensitive Graphene Biosensors Based on Surface Plasmon Resonance. Opt. Express 2010, 18 (14), 14395–14400. [PubMed: 20639924]

(54). Ferro MD; Melosh NA Electronic and Ionic Materials for Neurointerfaces. Adv. Funct. Mater 2018, 28 (12), 1704335.

(55). Chen H; Müller MB; Gilmore KJ; Wallace GG; Li D Mechanically Strong, Electrically Conductive, and Biocompatible Graphene Paper. Adv. Mater 2008, 20, 3557–3561.

(56). Wang F; Zhang Y; Tian C; Girit C; Zettl A; Crommie M; Shen YR Gate-Variable Optical Transitions in Graphene. Science 2008, 320, 206–209. [PubMed: 18339901]

(57). Horng J; Balch HB; McGuire AF; Tsai H-Z; Forrester PR; Crommie MF; Cui B; Wang F Imaging Electric Field Dynamics with Graphene Optoelectronics. Nat. Commun 2016, 7, 13704. [PubMed: 27982125]

(58). Liu Y; Chadha A; Zhao D; Piper JR; Jia Y; Shuai Y; Menon L; Yang H; Ma Z; Fan S; Xia F; Zhou W Approaching Total Absorption at near Infrared in a Large Area Monolayer Graphene by Critical Coupling. Appl. Phys. Lett 2014, 105 (18), 181105.

(59). Horng J; Balch H; McGuire A; Wang F; Cui B Electric Field Sensing with Graphene Optoelectronics for Action Potential Detection. In Conference on Lasers and Electro-Optics; OSA: Washington, D.C., 2018; p AM4P.2.

(60). Alfonso FS; Zhou Y; Liu E; McGuire AF; Yang Y; Kantarci H; Li D; Copenhaver E; Zuchero JB; Muller H; Cui B Label-Free Optical Detection of Bioelectric Potentials Using Electrochromic Thin Films. Proc. Natl. Acad. Sci. U. S. A 2020, 117 (29), 17260–17268. [PubMed: 32632007]

(61). Granqvist CG Electrochromic Tungsten Oxide Films: Review of Progress 1993–1998. Sol. Energy Mater. Sol. Cells 2000, 60 (3), 201–262.

(62). Cai G; Wang J; Lee PS Next-Generation Multifunctional Electrochromic Devices. Acc. Chem. Res 2016, 49 (8), 1469–1476. [PubMed: 27404116]

(63). Zhou Y; Li B; Li S; Ardoña HAM; Wilson WL; Tovar JD; Schroeder CM Concentration-Driven Assembly and Sol-Gel Transition of π-Conjugated Oligopeptides. ACS Cent. Sci 2017, 3 (9), 986–994. [PubMed: 28979940]

(64). Li B; Li S; Zhou Y; Ardoña HAM; Valverde LR; Wilson WL; Tovar JD; Schroeder CM Nonequilibrium Self-Assembly of π-Conjugated Oligopeptides in Solution. ACS Appl. Mater. Interfaces 2017, 9 (4), 3977–3984. [PubMed: 28067038]

(65). Li B; Valverde LR; Zhang F; Zhou Y; Li S; Diao Y; Wilson WL; Schroeder CM Macroscopic Alignment and Assembly of π-Conjugated Oligopeptides Using Colloidal Microchannels. ACS Appl. Mater. Interfaces 2017, 9 (47), 41586–41593. [PubMed: 29112374]

(66). Liu Y; McGuire AF; Lou H-Y; Li TL; Tok JB-H; Cui B; Bao Z Soft Conductive Micropillar Electrode Arrays for Biologically Relevant Electrophysiological Recording. Proc. Natl. Acad. Sci. U. S. A 2018, 115 (46), 11718–11723. [PubMed: 30377271]

(67). Khodagholy D; Gelinas JN; Thesen T; Doyle W; Devinsky O; Malliaras GG; Buzsáki G NeuroGrid: Recording Action Potentials from the Surface of the Brain. Nat. Neurosci 2015, 18 (2), 310–315. [PubMed: 25531570]

(68). Yu Z; Xia Y; Du D; Ouyang J PEDOT:PSS Films with Metallic Conductivity through a Treatment with Common Organic Solutions of Organic Salts and Their Application as a Transparent Electrode of Polymer Solar Cells. ACS Appl. Mater. Interfaces 2016, 8 (18), 11629–11638. [PubMed: 27113215]

(69). Richardson-Burns SM; Hendricks JL; Foster B; Povlich LK; Kim D-H; Martin DC Polymerization of the Conducting Polymer poly(3,4-Ethylenedioxythiophene) (PEDOT) around Living Neural Cells. Biomaterials 2007, 28 (8), 1539–1552. [PubMed: 17169420]

(70). Pires F; Ferreira Q; Rodrigues CAV; Morgado J; Ferreira FC Neural Stem Cell Differentiation by Electrical Stimulation Using a Cross-Linked PEDOT Substrate: Expanding the Use of Biocompatible Conjugated Conductive Polymers for Neural Tissue Engineering. Biochim. Biophys. Acta, Gen. Subj 2015, 1850 (6), 1158–1168.

(71). Marzocchi M; Gualandi I; Calienni M; Zironi I; Scavetta E; Castellani G; Fraboni B Physical and Electrochemical Properties of PEDOT:PSS as a Tool for Controlling Cell Growth. ACS Appl. Mater. Interfaces 2015, 7 (32), 17993–18003. [PubMed: 26208175]

(72). Ranjbar S; Nejad MAF; Parolo C; Shahrokhian S; Merkoçi A Smart Chip for Visual Detection of Bacteria Using the Electrochromic Properties of Polyaniline. Anal. Chem 2019, 91 (23), 14960–14966. [PubMed: 31682108]

(73). Wu J; Zhu Y; You L; Dong P; Mei J; Cheng J Polymer Electrochromism Driven by Metabolic Activity Facilitates Rapid and Facile Bacterial Detection and Susceptibility Evaluation. Adv. Funct. Mater 2020, 30, 2005192. [PubMed: 33708032]

(74). Nguyen C; Upadhyay H; Murphy M; Borja G; Rozsahegyi EJ; Barnett A; Brookings T; McManus OB; Werley CA Simultaneous Voltage and Calcium Imaging and Optogenetic Stimulation with High Sensitivity and a Wide Field of View. Biomed. Opt. Express 2019, 10 (2), 789–806. [PubMed: 30800515]

(75). Savagian LR; Osterholm AM; Ponder JF; Barth KJ; Rivnay J; Reynolds JR Balancing Charge Storage and Mobility in an Oligo(Ether) Functionalized Dioxythiophene Copolymer for Organic- and Aqueous-Based Electrochemical Devices and Transistors. Adv. Mater 2018, 30 (50), e1804647. [PubMed: 30368946]

(76). Doherty MW; Manson NB; Delaney P; Jelezko F; Wrachtrup J; Hollenberg LCL The Nitrogen-Vacancy Colour Centre in Diamond. Phys. Rep 2013, 528 (1), 1–45.

(77). Taylor JM; Cappellaro P; Childress L; Jiang L; Budker D; Hemmer PR; Yacoby A; Walsworth R; Lukin MD High-Sensitivity Diamond Magnetometer with Nanoscale Resolution. Nat. Phys 2008, 4 (10), 810–816.

(78). Steinert S; Dolde F; Neumann P; Aird A; Naydenov B; Balasubramanian G; Jelezko F; Wrachtrup J High Sensitivity Magnetic Imaging Using an Array of Spins in Diamond. Rev. Sci. Instrum 2010, 81 (4), 043705. [PubMed: 20441343]

(79). Pham LM; Le Sage D; Stanwix PL; Yeung TK; Glenn D; Trifonov A; Cappellaro P; Hemmer PR; Lukin MD; Park H; Yacoby A; Walsworth RL Magnetic Field Imaging with Nitrogen-Vacancy Ensembles. New J. Phys 2011, 13 (4), 045021.

(80). Le Sage D; Arai K; Glenn DR; DeVience SJ; Pham LM; Rahn-Lee L; Lukin MD; Yacoby A; Komeili A; Walsworth RL Optical Magnetic Imaging of Living Cells. Nature 2013, 496 (7446), 486–489. [PubMed: 23619694]

(81). Glenn DR; Lee K; Park H; Weissleder R; Yacoby A; Lukin MD; Lee H; Walsworth RL; Connolly CB Single-Cell Magnetic Imaging Using a Quantum Diamond Microscope. Nat. Methods 2015, 12 (8), 736–738. [PubMed: 26098019]

(82). Barry JF; Turner MJ; Schloss JM; Glenn DR; Song Y; Lukin MD; Park H; Walsworth RL Optical Magnetic Detection of Single-Neuron Action Potentials Using Quantum Defects in Diamond. Proc. Natl. Acad. Sci. U. S. A 2016, 113 (49), 14133–14138. [PubMed: 27911765]

(83). Dréau A; Lesik M; Rondin L; Spinicelli P; Arcizet O; Roch J-F; Jacques V Avoiding Power Broadening in Optically Detected Magnetic Resonance of Single NV Defects for Enhanced Dc Magnetic Field Sensitivity. Phys. Rev. B: Condens. Matter Mater. Phys 2011, 84, 195204.

(84). Hill DK The Volume Change Resulting from Stimulation of a Giant Nerve Fibre. J. Physiol 1950, 111 (3–4), 304–327. [PubMed: 14795441]

(85). Iwasa K; Tasaki I; Gibbons RC Swelling of Nerve Fibers Associated with Action Potentials. Science 1980, 210 (4467), 338–339. [PubMed: 7423196]

(86). Tasaki I; Iwasa K Rapid Pressure Changes and Surface Displacements in the Squid Giant Axon Associated with Production of Action Potentials. Jpn. J. Physiol 1982, 32 (1), 69–81. [PubMed: 6281506]

(87). Tasaki I; Kusano K; Byrne PM Rapid Mechanical and Thermal Changes in the Garfish Olfactory Nerve Associated with a Propagated Impulse. Biophys. J 1989, 55 (6), 1033–1040. [PubMed: 2765644]

(88). Tasaki I; Byrne PM Volume Expansion of Nonmyelinated Nerve Fibers during Impulse Conduction. Biophys. J 1990, 57 (3), 633–635. [PubMed: 2306506]

(89). Yao X-C; Rector DM; George JS Optical Lever Recording of Displacements from Activated Lobster Nerve Bundles and Nitella Internodes. Appl. Opt 2003, 42 (16), 2972–2978. [PubMed: 12790447]

(90). Kuznetsova TG; Starodubtseva MN; Yegorenkov NI; Chizhik SA; Zhdanov RI Atomic Force Microscopy Probing of Cell Elasticity. Micron 2007, 38 (8), 824–833. [PubMed: 17709250]

(91). Gonzalez-Perez A; Mosgaard LD; Budvytyte R; Villagran-Vargas E; Jackson AD; Heimburg T Solitary Electromechanical Pulses in Lobster Neurons. Biophys. Chem 2016, 216, 51–59. [PubMed: 27448851]

(92). Zhang PC; Keleshian AM; Sachs F Voltage-Induced Membrane Movement. Nature 2001, 413 (6854), 428–432. [PubMed: 11574890]

(93). Mosbacher J; Langer M; Hörber JK; Sachs F Voltage-Dependent Membrane Displacements Measured by Atomic Force Microscopy. J. Gen. Physiol 1998, 111 (1), 65–74. [PubMed: 9417135]

(94). Bockris JO; Reddy AKN Modern Electrochemistry: An Introduction to an Interdisciplinary Area; Springer Science & Business Media, 2012.

(95). Kim GH; Kosterin P; Obaid AL; Salzberg BM A Mechanical Spike Accompanies the Action Potential in Mammalian Nerve Terminals. Biophys. J 2007, 92 (9), 3122–3129. [PubMed: 17307820]

(96). El Hady A; Machta BB Mechanical Surface Waves Accompany Action Potential Propagation. Nat. Commun 2015, 6, 6697. [PubMed: 25819404]

(97). Engelbrecht J; Peets T; Tamm K Electromechanical Coupling of Waves in Nerve Fibres. Biomech. Model. Mechanobiol 2018, 17 (6), 1771–1783. [PubMed: 30032474]

(98). Kukura P; Ewers H; Müller C; Renn A; Helenius A; Sandoghdar V High-Speed Nanoscopic Tracking of the Position and Orientation of a Single Virus. Nat. Methods 2009, 6 (12), 923–927. [PubMed: 19881510]

(99). Park J-S; Lee I-B; Moon H-M; Joo J-H; Kim K-H; Hong S-C; Cho M Label-Free and Live Cell Imaging by Interferometric Scattering Microscopy. Chem. Sci 2018, 9 (10), 2690–2697. [PubMed: 29732052]

(100). Ling T; Boyle KC; Goetz G; Zhou P; Quan Y; Alfonso FS; Huang TW; Palanker D Full-Field Interferometric Imaging of Propagating Action Potentials. Light: Sci. Appl 2018, 7, 107. [PubMed: 30564313]

(101). Oh S; Fang-Yen C; Choi W; Yaqoob Z; Fu D; Park Y; Dassari RR; Feld MS Label-Free Imaging of Membrane Potential Using Membrane Electromotility. Biophys. J 2012, 103 (1), 11–18. [PubMed: 22828327]

(102). Hill B; Schubert E; Nokes M; Michelson R Laser Interferometer Measurement of Changes in Crayfish Axon Diameter Concurrent with Action Potential. Science 1977, 196, 426–428. [PubMed: 850785]

(103). Fang-Yen C; Chu MC; Seung HS; Dasari RR; Feld MS Noncontact Measurement of Nerve Displacement during Action Potential with a Dual-Beam Low-Coherence Interferometer. Opt. Lett 2004, 29 (17), 2028–2030. [PubMed: 15455769]

(104). Akkin T; Davé D; Milner T; Rylander H III Detection of Neural Activity Using Phase-Sensitive Optical Low-Coherence Reflectometry. Opt. Express 2004, 12 (11), 2377–2386. [PubMed: 19475074]

(105). LaPorta A; Kleinfeld D Interferometric Detection of Action Potentials. Cold Spring Harb. Protoc 2012, 2012 (3), 307–311. [PubMed: 22383643]

(106). Batabyal S; Satpathy S; Bui L; Kim Y-T; Mohanty S; Bachoo R; Davé DP Label-Free Optical Detection of Action Potential in Mammalian Neurons. Biomed. Opt. Express 2017, 8 (8), 3700–3713. [PubMed: 28856044]

(107). Ling T; Boyle KC; Zuckerman V; Flores T; Ramakrishnan C; Deisseroth K; Palanker D High-Speed Interferometric Imaging Reveals Dynamics of Neuronal Deformation during the Action Potential. Proc. Natl. Acad. Sci. U. S. A 2020, 117 (19), 10278–10285. [PubMed: 32341158]

(108). Kretschmann E; Raether H Notizen: Radiative Decay of Non Radiative Surface Plasmons Excited by Light. Z. Naturforsch., A: Phys. Sci 1968, 23 (12), 2135–2136.

(109). Huang B; Yu F; Zare RN Surface Plasmon Resonance Imaging Using a High Numerical Aperture Microscope Objective. Anal. Chem 2007, 79 (7), 2979–2983. [PubMed: 17309232]

(110). Homola J Surface Plasmon Resonance Sensors for Detection of Chemical and Biological Species. Chem. Rev 2008, 108 (2), 462–493. [PubMed: 18229953]

(111). Ae Kim S; Min Byun K; Lee J; Hoon Kim J; Albert Kim D-G; Baac H; Shuler ML; June Kim S Optical Measurement of Neural Activity Using Surface Plasmon Resonance. Opt. Lett 2008, 33 (9), 914–916. [PubMed: 18451937]

(112). Wang W; Wang S; Liu Q; Wu J; Tao N Mapping Single-Cell-Substrate Interactions by Surface Plasmon Resonance Microscopy. Langmuir 2012, 28 (37), 13373–13379. [PubMed: 22920036]

(113). Yang Y; Yu H; Shan X; Wang W; Liu X; Wang S; Tao N Label-Free Tracking of Single Organelle Transportation in Cells with Nanometer Precision Using a Plasmonic Imaging Technique. Small 2015, 11 (24), 2878–2884. [PubMed: 25703098]

(114). Wang S; Shan X; Patel U; Huang X; Lu J; Li J; Tao N Label-Free Imaging, Detection, and Mass Measurement of Single Viruses by Surface Plasmon Resonance. Proc. Natl. Acad. Sci. U. S. A 2010, 107 (37), 16028–16032. [PubMed: 20798340]

(115). Syal K; Iriya R; Yang Y; Yu H; Wang S; Haydel SE; Chen H-Y; Tao N Antimicrobial Susceptibility Test with Plasmonic Imaging and Tracking of Single Bacterial Motions on Nanometer Scale. ACS Nano 2016, 10 (1), 845–852. [PubMed: 26637243]

(116). Foley KJ; Shan X; Tao NJ Surface Impedance Imaging Technique. Anal. Chem 2008, 80 (13), 5146–5151. [PubMed: 18484741]

(117). Yuan L; Tao N; Wang W Plasmonic Imaging of Electrochemical Impedance. Annu. Rev. Anal. Chem 2017, 10 (1), 183–200.

(118). Wang W; Foley K; Shan X; Wang S; Eaton S; Nagaraj VJ; Wiktor P; Patel U; Tao N Single Cells and Intracellular Processes Studied by a Plasmonic-Based Electrochemical Impedance Microscopy. Nat. Chem 2011, 3 (3), 249–255. [PubMed: 21336333]

(119). Yang Y; Liu X-W; Wang H; Yu H; Guan Y; Wang S; Tao N Imaging Action Potential in Single Mammalian Neurons by Tracking the Accompanying Sub-Nanometer Mechanical Motion. ACS Nano 2018, 12 (5), 4186–4193. [PubMed: 29570267]

(120). Liu X-W; Yang Y; Wang W; Wang S; Gao M; Wu J; Tao N Plasmonic-Based Electrochemical Impedance Imaging of Electrical Activities in Single Cells. Angew. Chem., Int. Ed 2017, 56 (30), 8855–8859.

(121). Yang Y; Liu X; Wang S; Tao N Plasmonic Imaging of Subcellular Electromechanical Deformation in Mammalian Cells. J. Biomed. Opt 2019, 24, 1.

(122). Zhou X-L; Yang Y; Wang S; Liu X-W Surface Plasmon Resonance Microscopy: From Single-Molecule Sensing to Single-Cell Imaging. Angew. Chem., Int. Ed 2020, 59 (5), 1776–1785.

(123). Cohen LB; Keynes RD; Hille B Light Scattering and Birefringence Changes during Nerve Activity. Nature 1968, 218 (5140), 438–441. [PubMed: 5649693]

(124). Cohen LB; Keynes RD Changes in Light Scattering Associated with the Action Potential in Crab Nerves. J. Physiol 1971, 212, 259–275. [PubMed: 5545182]

(125). Cohen LB; Keynes RD; Landowne D Changes in Light Scattering That Accompany the Action Potential in Squid Giant Axons: Potential-Dependent Components. J. Physiol 1972, 224 (3), 701–725. [PubMed: 5071934]

(126). Cohen LB; Keynes RD; Landowne D Changes in Axon Light Scattering That Accompany the Action Potential: Current-Dependent Components. J. Physiol 1972, 224 (3), 727–752. [PubMed: 5071935]

(127). Stepnoski RA; LaPorta A; Raccuia-Behling F; Blonder GE; Slusher RE; Kleinfeld D Noninvasive Detection of Changes in Membrane Potential in Cultured Neurons by Light Scattering. Proc. Natl. Acad. Sci. U. S. A 1991, 88 (21), 9382–9386. [PubMed: 1946349]

(128). Lazebnik M; Marks DL; Potgieter K; Gillette R; Boppart SA Functional Optical Coherence Tomography for Detecting Neural Activity through Scattering Changes. Opt. Lett 2003, 28 (14), 1218–1220. [PubMed: 12885026]

(129). Park BH; Pierce MC; Cense B; Yun S-H; Mujat M; Tearney GJ; Bouma BE; de Boer JF Real-Time Fiber-Based Multi-Functional Spectral-Domain Optical Coherence Tomography at 13 μm. Opt. Express 2005, 13, 3931. [PubMed: 19495302]

(130). Akkin T; Joo C; de Boer JF Depth-Resolved Measurement of Transient Structural Changes during Action Potential Propagation. Biophys. J 2007, 93 (4), 1347–1353. [PubMed: 17526590]

(131). Yeh Y-J; Black AJ; Landowne D; Akkin T Optical Coherence Tomography for Cross-Sectional Imaging of Neural Activity. Neurophotonics 2015, 2 (3), 035001. [PubMed: 26217674]

(132). Graf BW; Ralston TS; Ko H-J; Boppart SA Detecting Intrinsic Scattering Changes Correlated to Neuron Action Potentials Using Optical Coherence Imaging. Opt. Express 2009, 17 (16), 13447–13457. [PubMed: 19654752]

(133). Habib A; Zhu X; Can UI; McLanahan ML; Zorlutuna P; Yanik AA Electro-Plasmonic Nanoantenna: A Nonfluorescent Optical Probe for Ultrasensitive Label-Free Detection of Electrophysiological Signals. Sci. Adv 2019, 5 (10), eaav9786. [PubMed: 31667339]

(134). Salzberg BM; Obaid AL; Gainer H Large and Rapid Changes in Light Scattering Accompany Secretion by Nerve Terminals in the Mammalian Neurohypophysis. J. Gen. Physiol 1985, 86 (3), 395–411. [PubMed: 2997364]

(135). Holthoff K; Witte OW Intrinsic Optical Signals in Rat Neocortical Slices Measured with near-Infrared Dark-Field Microscopy Reveal Changes in Extracellular Space. J. Neurosci 1996, 16 (8), 2740–2749. [PubMed: 8786449]

(136). Cohen LB; Hille B; Keynes RD Changes in Axon Birefringence during the Action Potential. J. Physiol 1970, 211 (2), 495–515. [PubMed: 5501012]

(137). Yao X-C; Foust A; Rector DM; Barrowes B; George JS Cross-Polarized Reflected Light Measurement of Fast Optical Responses Associated with Neural Activation. Biophys. J 2005, 88 (6), 4170–4177. [PubMed: 15805175]

(138). McCluskey MD; Sable JJ; Foust AJ; Gratton G; Rector DM Recording Invertebrate Nerve Activation with Modulated Light Changes. Appl. Opt 2007, 46 (10), 1866–1871. [PubMed: 17356632]

(139). Badreddine AH; Jordan T; Bigio IJ Real-Time Imaging of Action Potentials in Nerves Using Changes in Birefringence. Biomed. Opt. Express 2016, 7 (5), 1966–1973. [PubMed: 27231635]

(140). Foust AJ; Rector DM Optically Teasing Apart Neural Swelling and Depolarization. Neuroscience 2007, 145 (3), 887–899. [PubMed: 17303339]

(141). Sun C-K; Chu S-W; Chen S-Y; Tsai T-H; Liu T-M; Lin C-Y; Tsai H-J Higher Harmonic Generation Microscopy for Developmental Biology. J. Struct. Biol 2004, 147 (1), 19–30. [PubMed: 15109602]

(142). Chen S-Y; Hsieh C-S; Chu S-W; Lin C-Y; Ko C-Y; Chen Y-C; Tsai H-J; Hu C-H; Sun C-K Noninvasive Harmonics Optical Microscopy for Long-Term Observation of Embryonic Nervous System Development in Vivo. J. Biomed. Opt 2006, 11 (5), 054022. [PubMed: 17092171]

(143). Débarre D; Supatto W; Pena A-M; Fabre A; Tordjmann T; Combettes L; Schanne-Klein M-C; Beaurepaire E Imaging Lipid Bodies in Cells and Tissues Using Third-Harmonic Generation Microscopy. Nat. Methods 2006, 3 (1), 47–53. [PubMed: 16369553]

(144). Witte S; Negrean A; Lodder JC; de Kock CPJ; Testa Silva G; Mansvelder HD; Louise Groot M Label-Free Live Brain Imaging and Targeted Patching with Third-Harmonic Generation Microscopy. Proc. Natl. Acad. Sci. U. S. A 2011, 108 (15), 5970–5975. [PubMed: 21444784]

(145). Gonella G; Lütgebaucks C; de Beer AGF; Roke S Second Harmonic and Sum-Frequency Generation from Aqueous Interfaces Is Modulated by Interference. J. Phys. Chem. C 2016, 120 (17), 9165–9173.

(146). Lütgebaucks C; Gonella G; Roke S Optical Label-Free and Model-Free Probe of the Surface Potential of Nanoscale and Microscopic Objects in Aqueous Solution. Phys. Rev. B: Condens. Matter Mater. Phys 2016, 94 (19), 195410.

(147). Tarun OB; Hannesschläger C; Pohl P; Roke S Label-Free and Charge-Sensitive Dynamic Imaging of Lipid Membrane Hydration on Millisecond Time Scales. Proc. Natl. Acad. Sci. U. S. A 2018, 115 (16), 4081–4086. [PubMed: 29610320]

(148). Didier MEP; Tarun OB; Jourdain P; Magistretti P; Roke S Membrane Water for Probing Neuronal Membrane Potentials and Ionic Fluxes at the Single Cell Level. Nat. Commun 2018, 9 (1), 5287. [PubMed: 30538243]

(149). Movasaghi Z; Rehman S; Rehman IU Raman Spectroscopy of Biological Tissues. Appl. Spectrosc. Rev 2007, 42 (5), 493–541.

(150). Palonpon AF; Ando J; Yamakoshi H; Dodo K; Sodeoka M; Kawata S; Fujita K Raman and SERS Microscopy for Molecular Imaging of Live Cells. Nat. Protoc 2013, 8 (4), 677–692. [PubMed: 23471112]

(151). Min W; Freudiger CW; Lu S; Xie XS Coherent Nonlinear Optical Imaging: Beyond Fluorescence Microscopy. Annu. Rev. Phys. Chem 2011, 62, 507–530. [PubMed: 21453061]

(152). Cheng J-X; Xie XS Vibrational Spectroscopic Imaging of Living Systems: An Emerging Platform for Biology and Medicine. Science 2015, 350 (6264), aaa8870. [PubMed: 26612955]

(153). Lee HJ; Zhang D; Jiang Y; Wu X; Shih P-Y; Liao C-S; Bungart B; Xu X-M; Drenan R; Bartlett E; Cheng J-X Label-Free Vibrational Spectroscopic Imaging of Neuronal Membrane Potential. J. Phys. Chem. Lett 2017, 8 (9), 1932–1936. [PubMed: 28407470]

(154). Liu B; Lee HJ; Zhang D; Liao C-S; Ji N; Xia Y; Cheng J-X Label-Free Spectroscopic Detection of Membrane Potential Using Stimulated Raman Scattering. Appl. Phys. Lett 2015, 106 (17), 173704.

(155). Lee HJ; Jiang Y; Cheng J-X Label-Free Optical Imaging of Membrane Potential. Current Opinion in Biomedical Engineering 2019, 12, 118–125. [PubMed: 32864527]

(156). Liu R; Zhao S; Liu J From Lithographically Patternable to Genetically Patternable Electronic Materials for Miniaturized, Scalable, and Soft Implantable Bioelectronics to Interface with Nervous and Cardiac Systems. ACS Applied Electronic Materials 2021, 3, 101–118.

(157). Dombeck DA Optical Recording of Action Potentials with Second-Harmonic Generation Microscopy. J. Neurosci 2004, 24, 999–1003. [PubMed: 14749445]

(158). Macias-Romero C; Didier MEP; Jourdain P; Marquet P; Magistretti P; Tarun OB; Zubkovs V; Radenovic A; Roke S High Throughput Second Harmonic Imaging for Label-Free Biological Applications. Opt. Express 2014, 22 (25), 31102–31112. [PubMed: 25607059]

(159). Xia F; Wu C; Sinefeld D; Li B; Qin Y; Xu C Label-Free Confocal Imaging of the Deep Mouse Brain with Long-Wavelength Illumination. Biomed. Opt. Express 2018, 9 (12), 6545–6555. [PubMed: 31065448]

(160). Oh G; Chung E; Yun SH Optical Fibers for High-Resolution in Vivo Microendoscopic Fluorescence Imaging. Opt. Fiber Technol 2013, 19 (6), 760–771.

(161). Pisanello F; Mandelbaum G; Pisanello M; Oldenburg IA; Sileo L; Markowitz JE; Peterson RE; Della Patria A; Haynes TM; Emara MS; Spagnolo B; Datta SR; De Vittorio M; Sabatini BL Dynamic Illumination of Spatially Restricted or Large Brain Volumes via a Single Tapered Optical Fiber. Nat. Neurosci 2017, 20 (8), 1180–1188. [PubMed: 28628101]

(162). Boyden ES; Zhang F; Bamberg E; Nagel G; Deisseroth K Millisecond-Timescale, Genetically Targeted Optical Control of Neural Activity. Nat. Neurosci 2005, 8 (9), 1263–1268. [PubMed: 16116447]

(163). Cohen AE; Farhi SL Sculpting Light to Reveal Brain Function. Nat. Neurosci 2018, 21 (6), 776–778. [PubMed: 29802389]
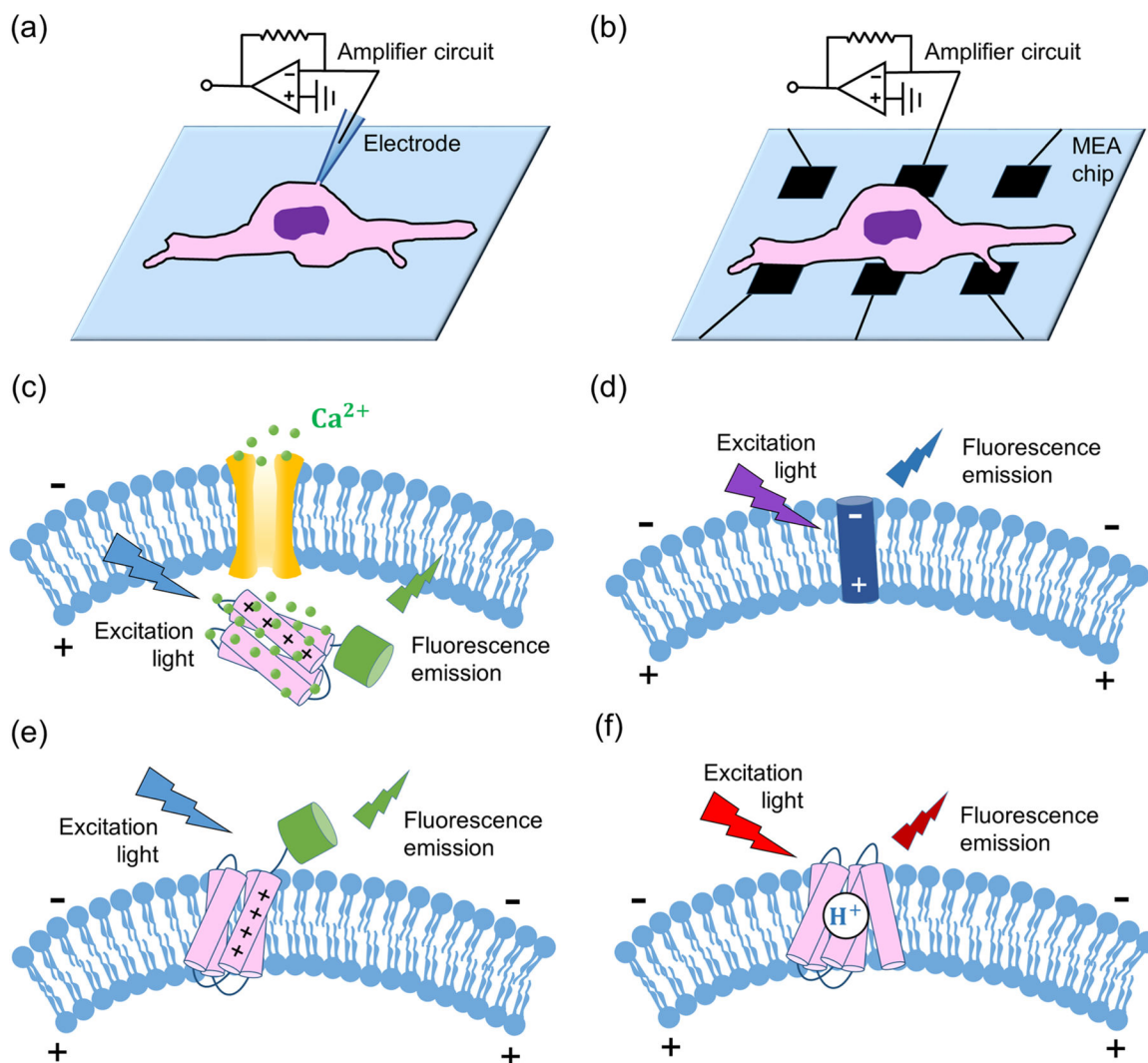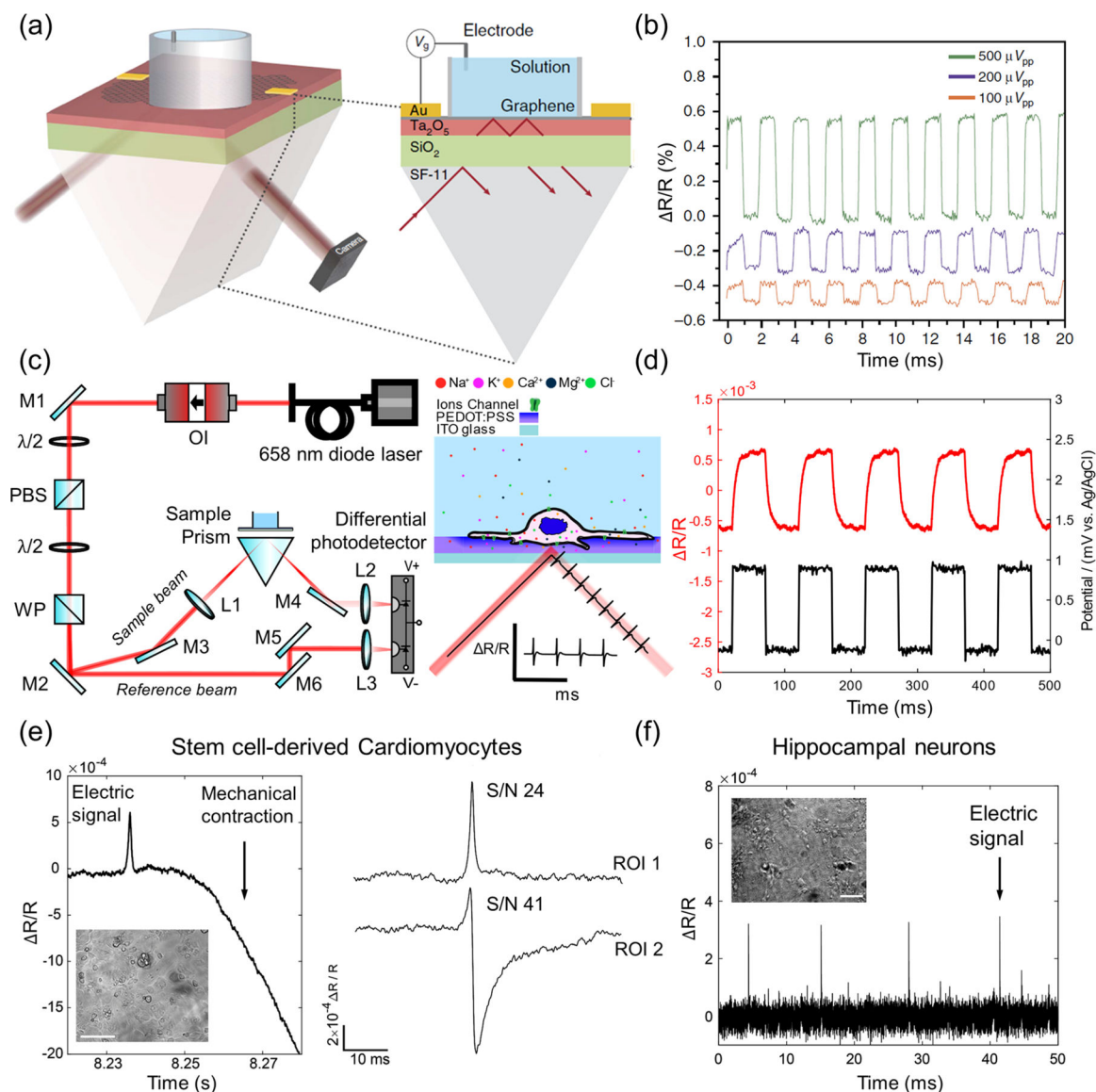
Figure 1.
Electrode-based and fluorescence-based electrophysiology techniques. (a) Schematic of whole-cell patch clamp. (b) Schematic of multi-electrode array (MEA). (c) Schematic of a genetically encoded calcium indicator. (d) Schematic of a voltage sensitive small molecule dye inserted into the cell membrane. (e) Schematic of a genetically encoded voltage indicator that fuses a voltage sensitive domain (pink) and a fluorescent protein (green) together. (f) Schematic of a genetically encoded voltage indicator based on microbial rhodopsin.

Figure 2.

Electrochromic recording–imaging action potentials using thin films of electrochromic materials. (a) Schematic of a graphene-based electrical-field imaging platform. The transverse electric-polarized collimated incident beam is coupled through a SiO_2 coated prism (green) and a Ta_2O_5 waveguide (red) to probe the graphene layer (gray) at the interface with aqueous solution. The beam incident angle is finely adjusted to achieve critical coupled condition and the output beam from the prism is detected by an InGaAs photodiode and/or camera. (b) Detected reflectance change of graphene layers when square waves of different voltages are applied. (c) Schematic of prism-based TIR ECORE setup. OI: optical isolator, M: mirror, $\lambda/2$: half-wave plate, PBS: polarizing beam splitter, WP: Wollaston prism, L: lens (left). Schematic of ECORE recording of cell membrane potentials (right). (d) Detected reflectance change when 1 mV square wave is applied to the PEDOT:PSS film. (e) Electrical signal and mechanical contraction of cardiomyocytes detected from ECORE (left). ECORE optical recording detects cardiomyocyte signals

with high SNR (right). Bright-field image of stem cell-derived cardiomyocytes cultured on a PEDOT:PSS film. Scale bar = 250 μm (inset). (f) Electrical signals of hippocampal neurons detected from ECORE. Bright-field image of hippocampal neurons cultured on a PEDOT:PSS film. Scale bar = 100 μm (inset). Panels a and b reproduced with permission from ref 57 under a Creative Commons Attribution License 4.0 (CC BY 4.0). Copyright 2016 Springer Nature. Panels c–f adapted with permission from ref 60. Copyright 2020 PNAS.
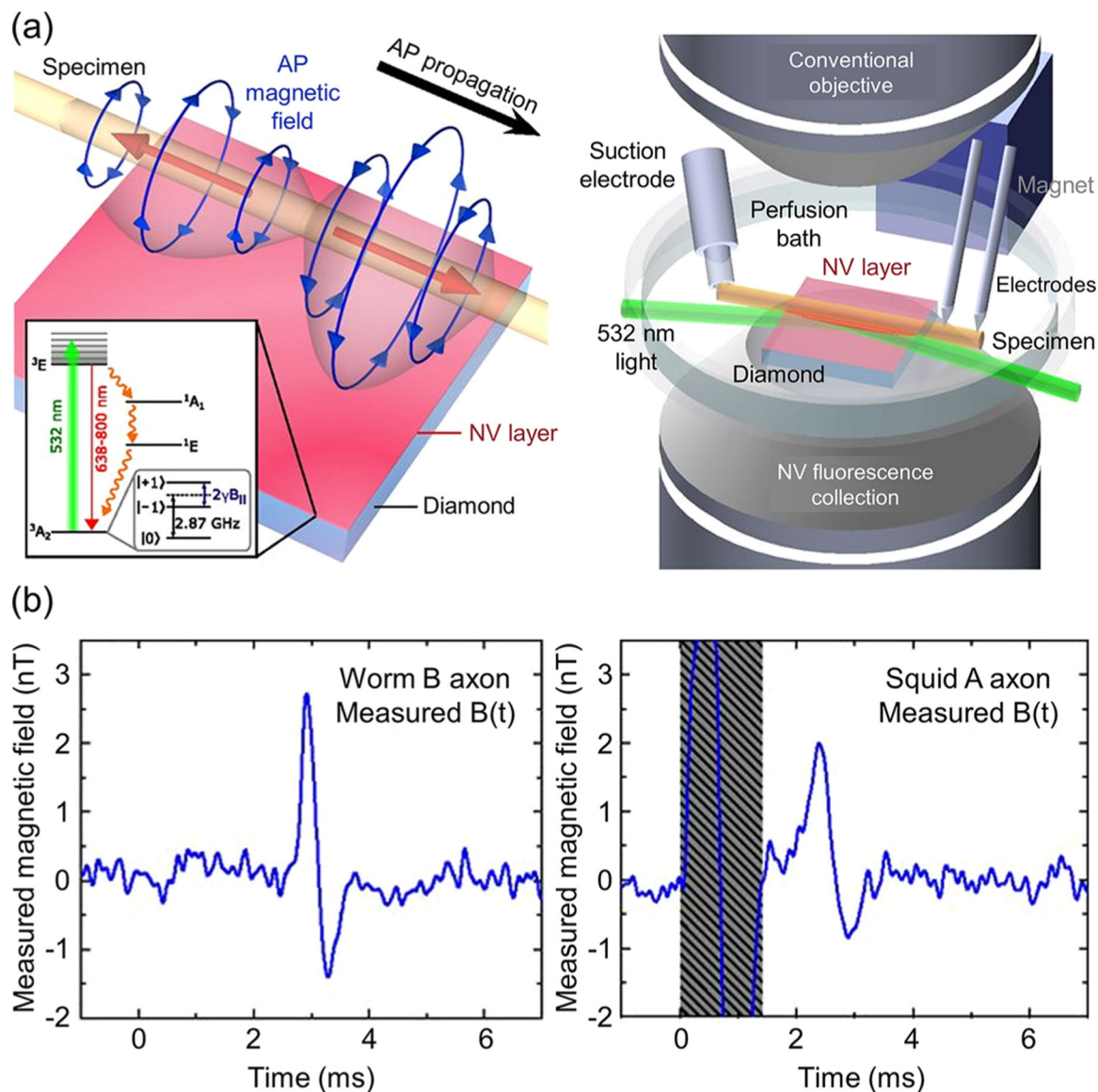
Figure 3.
Imaging action potentials by nitrogen-vacancy centers in diamonds. (a) Schematic of bipolar azimuthal magnetic field (blue arrows) accompanied by propagating action potential from left to right (left). The red arrows indicate the current passing through the axon. The specimen is placed on a 13-μm-thick single-crystal diamond chip doped with high density NV centers. The inset shows the NV center energy level diagram. Schematic of a quantum diamond microscopy set up (right). Magnetic field sensing and conventional imaging can be performed. The NV spin states are probed using a 532 nm green laser, and the laser-induced fluorescence in red is collected. Constant 7-G bias magnetic field is applied to the diamond by the magnets. Action potentials are stimulated using the suction electrode and recorded using bipolar electrodes. (b) Time trace of measured magnetic field B(t) associated with action potential from *M. infundibulum* giant axon with averaging of 600 traces (left), and from squid giant axon with averaging of 375 traces (right). A magnetic artifact resulting

from stimulation current is indicated in the gray box. Adapted with permission from ref 82. Copyright 2016 PNAS.
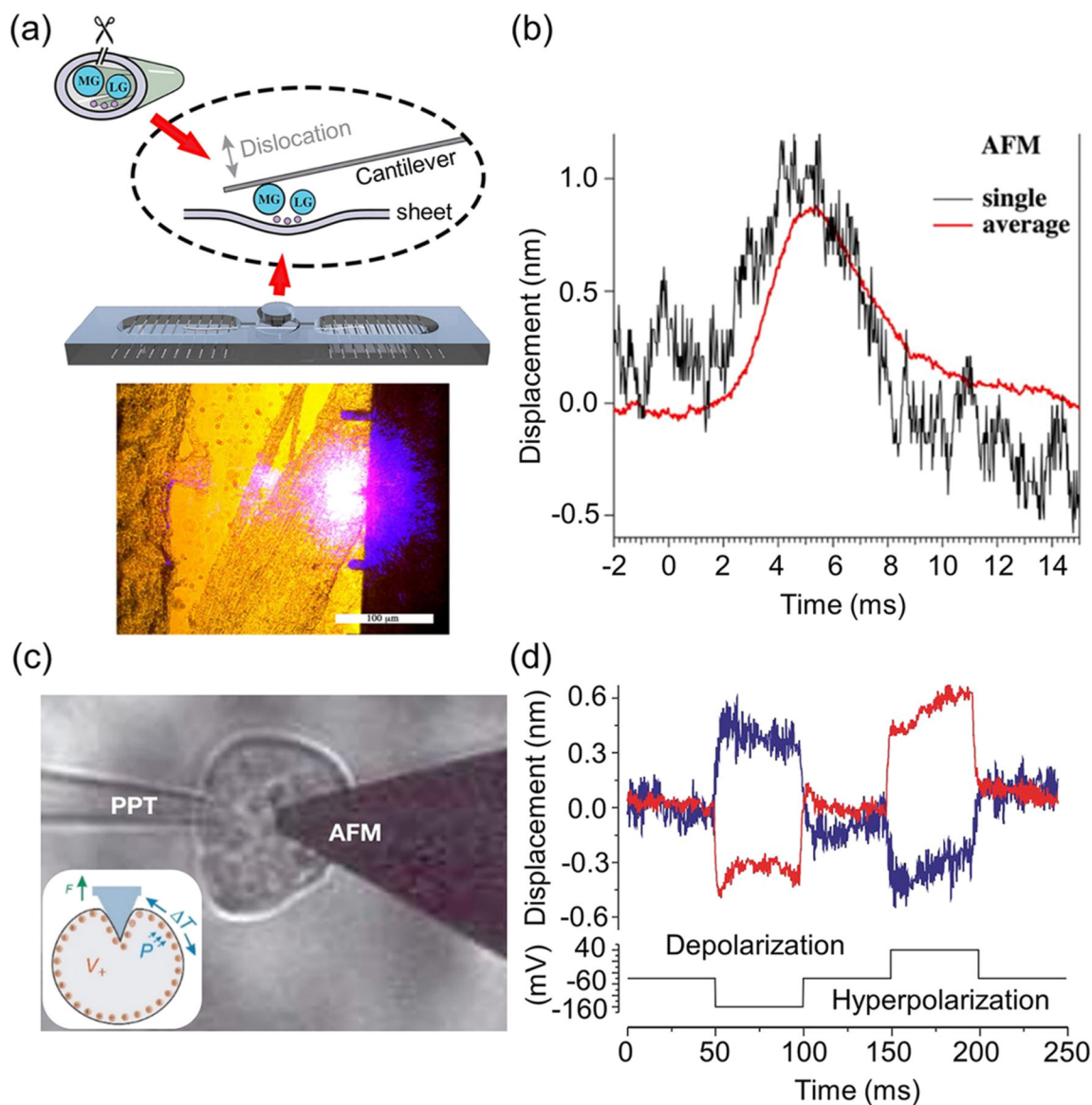
Figure 4.
Detecting electrical-depolarization-induced membrane deformations using AFM. (a) Schematic of AFM measurement on giant lobster axons (top). Microscope view of placement of AFM cantilever on the giant lobster axon with laser on. Scale bar = 100 μm (bottom). (b) Recorded axon membrane changes from a single trace and signals after averaging 100 traces. (c) Voltage clamped HEK 293 cell with AFM cantilever and glass pipet in place. (d) Membrane moves outward under 100 mV depolarization potential and inward under 100 mV hyperpolarization potential at normal (blue) ionic strengths. This behavior is reversed at 0 mM (red) ionic strengths. Panels a and b adapted with permission from ref 91. Copyright 2016 Elsevier. Panels c and d adapted with permission from ref 92. Copyright 2001 Springer Nature.
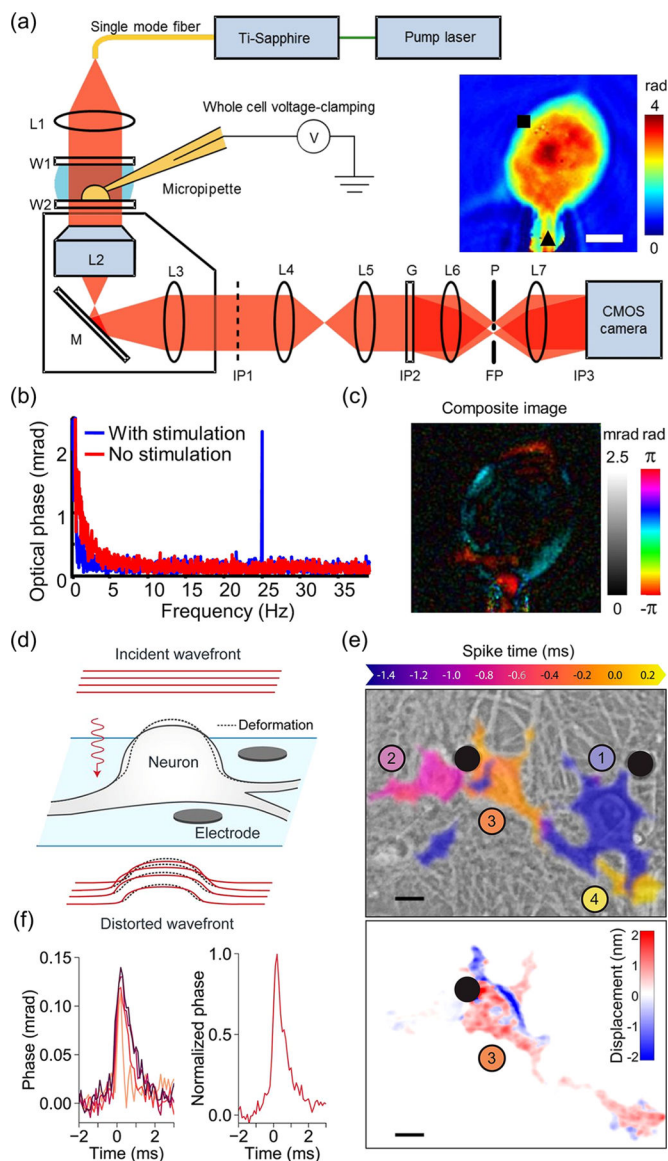
Figure 5.
Imaging action potential-induced membrane deformations by interferometric microscopy. (a) Set up of low-coherence diffraction phase microscope (LCDPM). L: lenses, W: cover glass, M: mirror, G: grating, P: pinhole and aperture, IP: image planes, FP: Fourier plane. Inset: phase image of HEK 293 cell. The color bar denotes phase in radians. The back triangle denotes the patch-clamp pipet position. Scale bar = 10 μm. (b) Optical phase spectrum of HEK 293 cell with (blue) and without (red) 25 Hz electrical stimulation from the area marked in the back square in the inset of (a). (c) Optical phase fluctuation image composed of the amplitude (mrad scale) and the time delay (rad scale) of the signal relative to the electrical stimulation at 25 Hz. (d) A neuron plated on transparent MEA substrate with simultaneous interferomic voltage imaging. Collimated incident wavefront is distorted with phase changes after passing through the neuron. (e) Detected spike time for neurons across the field of view (top). Membrane displacement in the third neuron at 0 ms (bottom). The

black circles indicate the position of the MEA electrode. Scale bar = 10 μm. (f) Individual (left) and averaged (right) time dependent phase signals of four neurons. An average quick phase change of 0.12 mrad is observed followed by a 1–2 ms relaxation (right). Panels a–c adapted with permission from ref 101. Copyright 2012 Elsevier. Panels d–f adapted with permission from ref 107. Copyright 2020 PNAS.
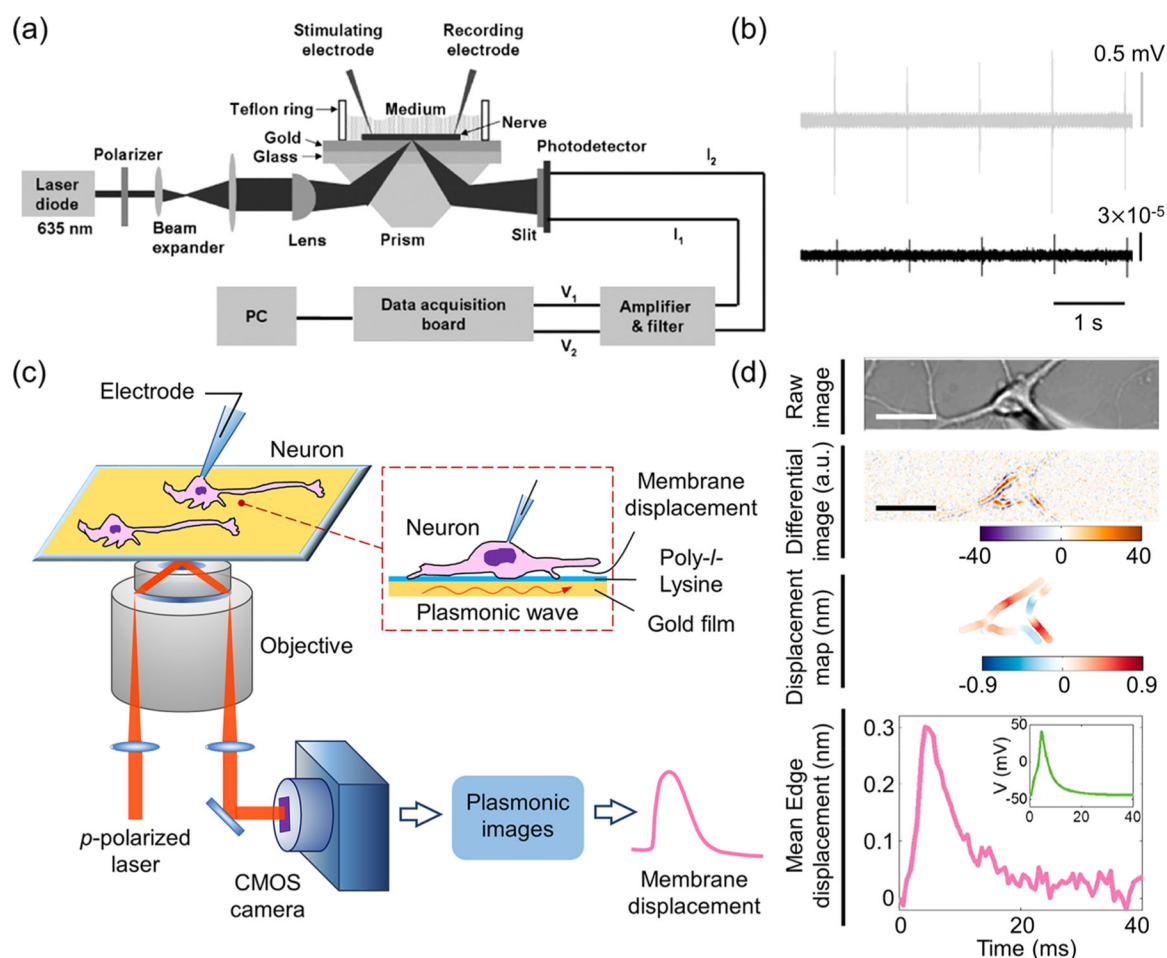
Figure 6.
Imaging action potential-induced membrane deformations by surface plasmon resonance microscopy. (a) Schematic of a prism-based surface plasmon resonance (SPR) setup to detect nerve activities. (b) Electrode recorded nerve electrical signal (gray) and optically recorded optical responses (black) of a rat sciatic nerve under 1 mA electrical stimulus. (c) Schematic of a plasmon-based electrochemical impedance microscope set up. Neurons are cultured on poly-*l*-lysine coated gold-coated glass coverslip and *p*-polarized laser is used to excite surface plasmons through a high N.A. objective. Plasmonic images are taken using a CMOS camera. A patch clamp electrode is attached to the neuron for recording and stimulation of membrane potentials. (d) Membrane displacement accompanied by action potentials for a neuron. The displacements are detected from SPR images using a differential detection algorithm and are mapped over the neuron membrane. Mean membrane displacement is extracted from the displacement profile and the time course matches well with the simultaneous electrode recorded action potential. Scale bars = 15 μm. Panels a and b adapted with permission from ref 111. Copyright 2008 The Optical Society. Panel d adapted with permission from ref 119. Copyright 2018 American Chemical Society.
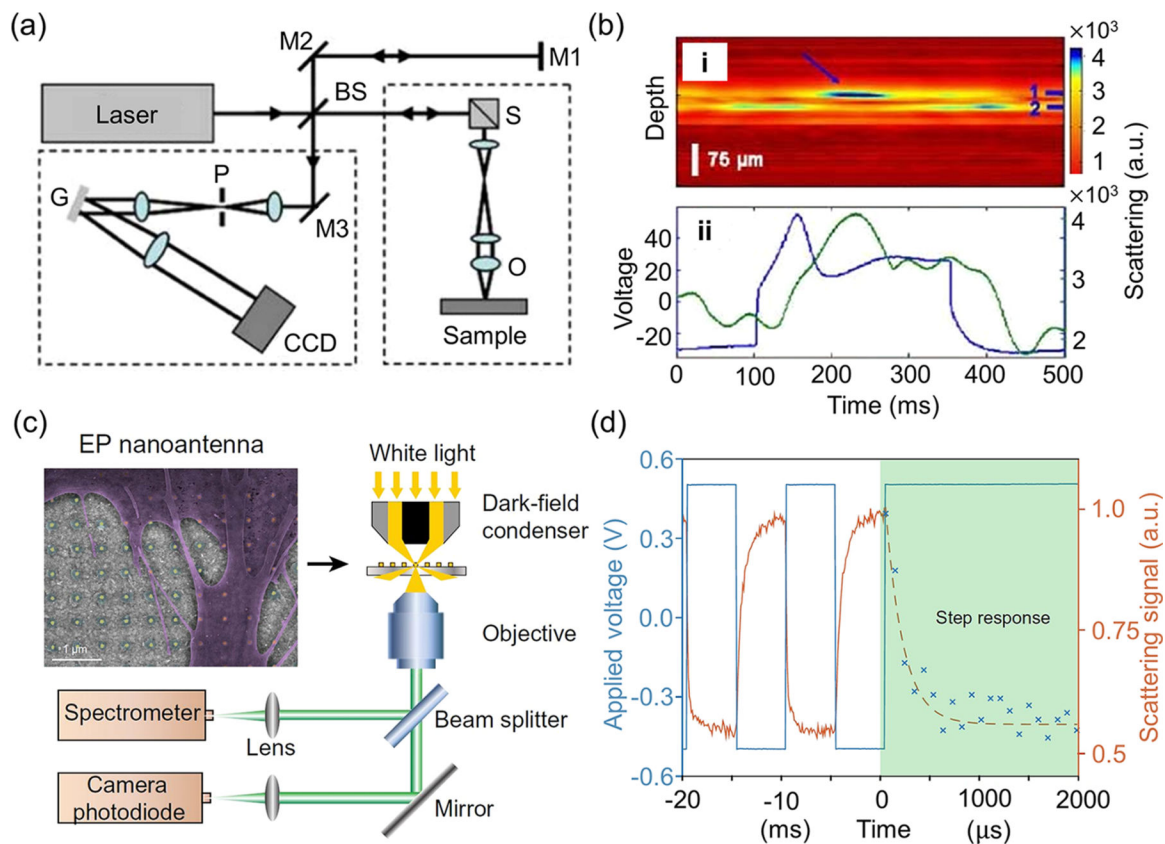
Figure 7.
Imaging action potentials through light scattering changes. (a) Schematic of a SD-OCT/OCM system. Laser beam is split by a beamsplitter (BS) into a reference arm and a sample arm. Laser beams from the reference arm and the sample arm are combined to form an interference pattern that is detected by a spectrometer consisting of a differential grating (G) and a line scan charge-coupled device (CCD) camera. The OCT/OCM image is constructed by moving the beam across the sample using galvanometer-driven scanning mirrors (S). M: mirror, O: objective. (b) (i) The scattering image from the neuron top surface is indicated at position 1. The blue arrow indicates an increase in scattering intensity accompanied by the action potential. The reflection from the culture dish is indicated at position 2. (ii) Scattering change (green) and applied membrane voltage (blue) of the neuron. The data is averaged over 25 trials. (c) Schematic of dark-field microscopy setup to detect the far-field scattering signal from the cells on the electroplasmonic (EP) nanoantenna array. Inset: electron micrograph of cardiomyocytes cultured on an EP nanoantenna array. (d) Light scattering signal response of the EP nanoantenna (orange) under 200 Hz, 1 V potential steps (blue) with a switching time of 191 μs. Panels a and b adapted with permission from ref 132. Copyright 2009 The Optical Society. Panels c and d adapted with permission from ref 133. Copyright Habib et al., some rights reserved; exclusive licensee AAAS. Distributed under a Creative Commons Attribution NonCommercial License 4.0 (CC BY-NC).
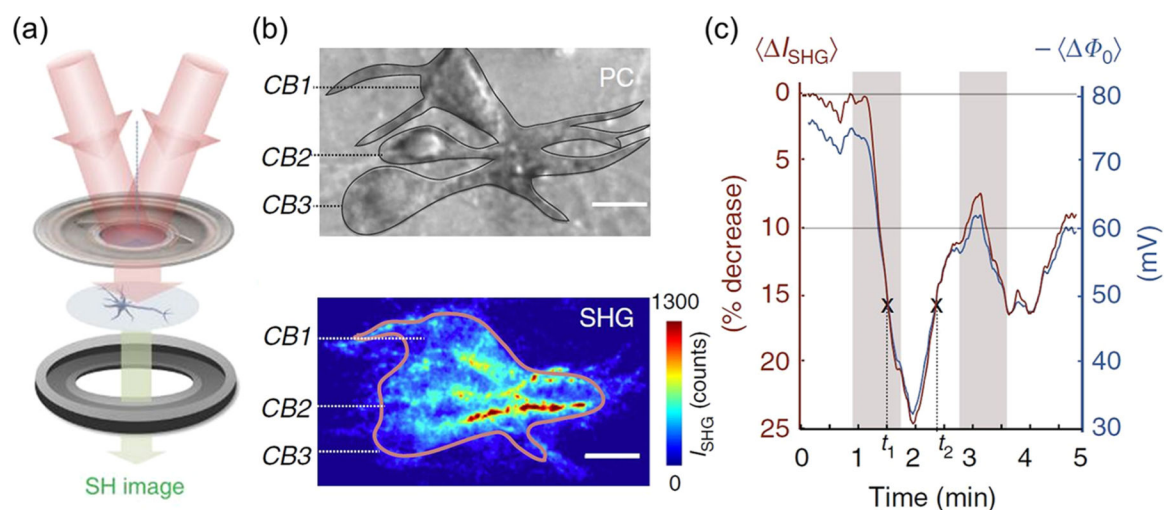
Figure 8.
Imaging cell electrical signals using second harmonic generation microscopy. (a) Schematic of second harmonic generation (SHG) imaging setup using a wide-field double beam transmission geometry. (b) Phase contrast (PC) image (top) and SHG image (bottom) of three cell bodies (CBs) of mouse cortical neurons. Heterogeneities in cell bodies during the depolarization step are observed in the SHG image. The area where the membrane potential calculations were made is enclosed in the colored contour. (c) Spatially averaged second harmonic signal (left axis) and computationally calculated membrane potentials (right axis) as a function of time during potassium induced membrane depolarization. The gray zones indicate the time windows when potassium enriched solution is added. Adapted with permission from ref 148 under a Creative Commons Attribution License 4.0 (CC BY 4.0). Copyright 2018 Springer Nature.
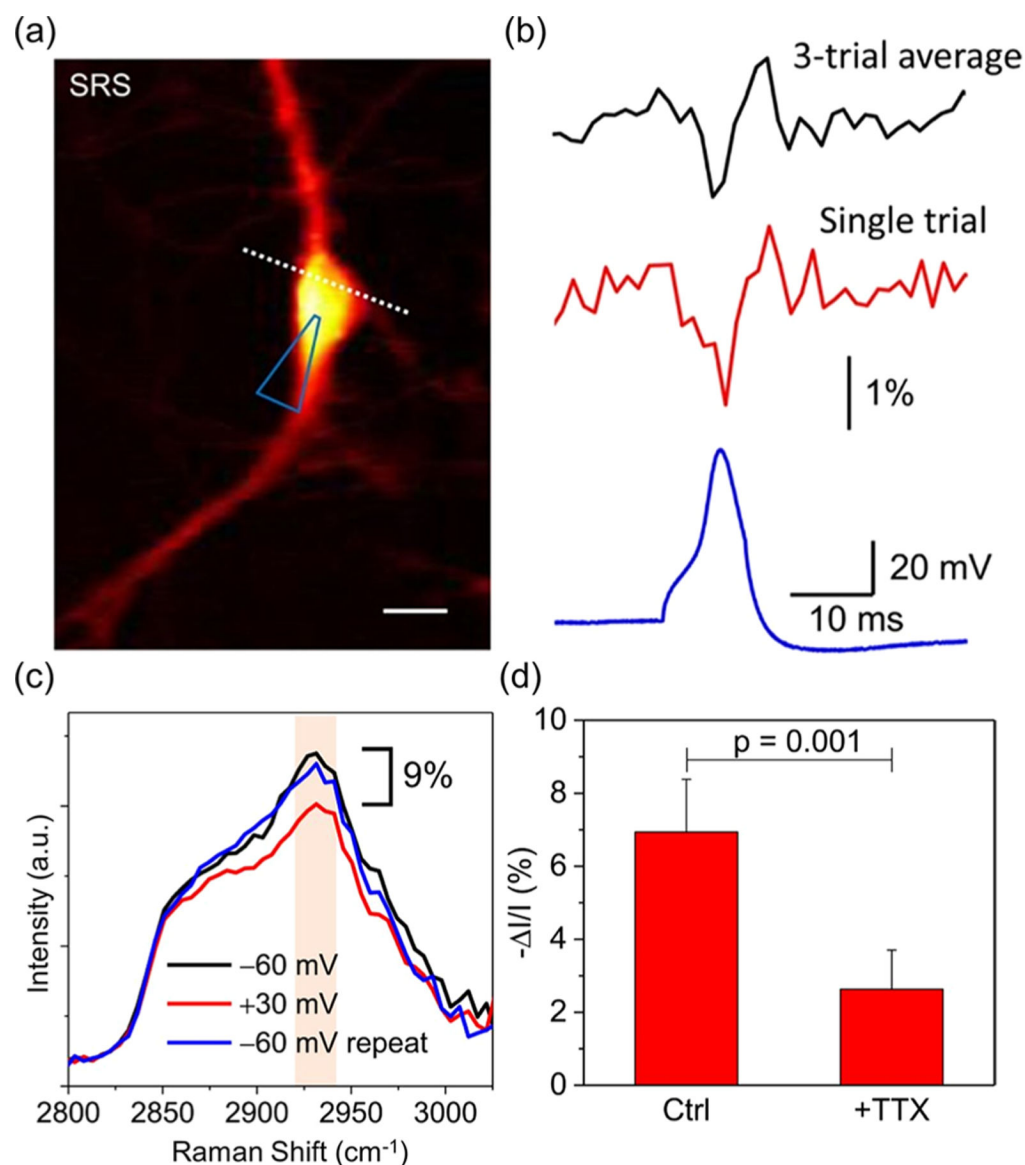
Figure 9.
Imaging cellular action potentials using stimulated Raman scattering microscopy. (a) SRS image of a mouse cortex neuron. The dashed line indicates the SRS scanning trace. The blue triangle denotes the patch-clamp pipet position. Scale bar = 20 μm. (b) Three-trial average (black) and single-trial (red) SRS signal of the neurons. Single action potential is also recorded by simultaneous current clamp recording (blue). The SRS signals were normalized by the reference SRS signals under the same electrical pulses. (c) SRS spectra of a mouse cortex neuron recorded at membrane potentials of −60 and +30 mV. Vibrational spectrum at ~2930 cm^{-1} (pink zone) from −CH$_3$ groups in membrane proteins mainly contributes to the changes in SRS intensity. (d) Changes of SRS intensity of neurons at 2930 cm^{-1} under +30 mV depolarization membrane potential before and after 3 μM tetrodotoxin (TTX) treatment. Adapted with permission from ref 153. Copyright 2017 American Chemical Society.

Table 1.

Recent Advances in Label-Free Optical Electrophysiology

sensing mechanism	sensing methods	biological specimen	year	SNR	detection limit	signal bandwidth	near-field/far-field detection
voltage-induced color change in electrochromic materials	ECORE	stem cell-derived cardiomyocyte, rat hippocampal neuron/brain slice	2020[60]	24–41	6.7 μV extracellular potential from single event	5 kHz, 300 Hz	near-field
action potential accompanied magnetic field	quantum diamond microscopy	worm and squid giant axon	2016[82]	>1	34 nT·μm$^{3/2}$·Hz$^{-1/2}$ magnetic field by averaging hundreds to thousands events	3.6 kHz	near-field
membrane deformation	AFM	mouse neurohypophysis	2007[95]	>25	5–10 nm deformation from single event	7 kHz	near-field
		lobster giant axon	2016[91]	N/A	<1 nm deformation by averaging 100 events	3 kHz	near-field
	SPR	rat hippocampal neuron	2018[119]	7	<1 nm deformation from single event	1603 Hz	near-field
	interferometric imaging	HEK 293 cell	2012[101]	N/A	~mrad phase change from single event	500 Hz	far-field
			2018[100]	47.7 dB	0.3 mrad/pixel phase change by averaging thousands events	1 kHz	
		rat cortical neuron	2017[106]	N/A	0.05 nm in optical path difference	200–300 Hz	
			2020[107]	21.5	4 pm/pixel deformation by averaging thousands events	10 kHz	
membrane scattering change	OCT/OCM	*Aplysia californica* bag cell neuron	2009[132]	N/A	single action potential by averaging 25 events	1 kHz (line scan rate)	far-field
	dark-field microscopy with nanoantenna	stem cell-derived cardiomyocyte	2019[133]	~60	200 V/cm^2 potential from single event	1 kHz	near-field
membrane water molecules reorientation	SHG microscopy	mouse cortical neuron	2018[148]	4	long-term membrane depolarization from single event	1.67 Hz	far-field
membrane protein –CH$_3$ vibrational modes	SRS microscopy	mouse cortex neuron/brain slice	2017[153]	3.6	single action potential from single event	1 kHz (line scan rate)	far-field